J. Fluid Mech. (2009), *vol.* 639, *pp.* 291–341.
doi:10.1017/S0022112009991066

Characterization of stationary mixing patterns in a three-dimensional open Stokes flow: spectral properties, localization and mixing regimes

M. GIONA†, S. CERBELLI AND F. GAROFALO

Dipartimento di Ingegneria Chimica,
Sapienza Università di Roma, via Eudossiana 18, 00184 Rome, Italy

(Received 26 August 2008; revised 2 July 2009; accepted 2 July 2009; first published online 13 October 2009)

This article analyses stationary scalar mixing downstream an open flow Couette device operating in the creeping flow regime. The device consists of two coaxial cylinders of finite length L_z, and radii κR and R ($\kappa < 1$), which can rotate independently. At relatively large values of the aspect ratio $\alpha = L_z/R \gg 1$, and of the Péclet number Pe, the stationary response of the system can be accurately described by enforcing the simplifying assumption of negligible axial diffusion. With this approximation, homogenization along the device axis can be described by a family of generalized one-dimensional eigenvalue problems with the radial coordinate as independent variable. A variety of mixing regimes can be observed by varying the geometric and operating parameters. These regimes are characterized by different localization properties of the eigenfunctions and by different scaling laws of the real part of the eigenvalues with the Péclet number. The analysis of this model flow reveals the occurrence of sharp transitions between mixing regimes, e.g. controlled by the geometric parameter κ. The eigenvalue scalings can be theoretically predicted by enforcing eigenfunction localization and simple functional equalities relating the behaviour of the eigenvalues to the functional form of the associated eigenfunctions. Several flow protocols corresponding to different geometric and operating conditions are considered. Among these protocols, the case where the inner and the outer cylinders counter-rotate exhibits a peculiar intermediate scaling regime where the real part of the dominant eigenvalue is independent of Pe over more than two decades of Pe. This case is thoroughly analysed by means of scaling analysis. The practical relevance of the results deriving from spectral analysis for fluid mixing problems in finite-length Couette devices is addressed in detail.

1. Introduction

The evolution of a scalar field in a laminar flow admits a wealth of practical and theoretical implications in chemical and mechanical engineering (Baldyga & Bourne 1999; Pelesko & Bernstein 2003), meteorology (Shepherd, Koshyk & Ngan 2000), biotechnology (Beebe, Mensing & Walker 2002; Raynal *et al.* 2007), geology (Perugini, Poli & Mazzuoli 2003) and environmental biology (Scheuring *et al.* 2000, 2003). The physical phenomenology underlying the evolution of a scalar field (be it

† Email address for correspondence: max@giona.ing.uniroma1.it

the concentration of a tracer, temperature, etc.) in a moving continuum is customarily referred to as fluid mixing.

In all of the cases where the coupling between the evolution of the scalar field and the momentum transport equation of the carrier flow can be neglected (the two transport equations are typically coupled by the dependence of density and viscosity on the scalar concentration), the mixing dynamics of the scalar field is governed by the interplay between advection and diffusion, quantitatively described by the linear advection–diffusion equation

$$\frac{\partial \phi}{\partial t} = -\nabla \cdot (\mathbf{v}\phi) + \mathscr{D}\,\nabla^2 \phi, \tag{1.1}$$

where ϕ is the concentration of the (scalar) transported entity, $\mathbf{v}$ the velocity field and $\mathscr{D}$ the diffusion coefficient. Equation (1.1) must be equipped with proper initial and boundary conditions, which depend on the specific flow problem considered, on the nature of the flow domain and on the initial profile of the scalar field.

A simple way to categorize different fluid mixing problems can be grounded on the nature of the flow domain. In this framework, three main categories can be identified, namely (i) infinitely extended flow domains, (ii) closed bounded flows and (iii) open bounded flows.

In unbounded flow domains, fluid mixing is equivalent to *dispersion*, where the properties of a scalar tracer are characterized in a long-time long-distance perspective. Examples of physical processes where this approach is sensibly applied are environmental pollutant dispersion in large-scale oceanographic analysis, or ecosystem stability studies to unveil the effect of fluid streams. The theoretical analysis of dispersion can be tackled either by means of probabilistic methods, or through homogenization techniques (Bensoussan, Lions & Papanicolau 1978; Fannjiang & Papanicolaou 1994; Majda & Kramer 1999). Typical flow models in infinitely extended domains involve either cellular flows (Fannjiang & Papanicolaou 1994) or infinitely long tubes, such as in the analysis of Taylor–Aris dispersion in capillaries (Taylor 1953; Aris 1956).

In finite-sized domains delimited by impermeable boundaries (closed flows), the large-scale analysis of the spatial structure of an evolving scalar field is intrinsically meaningless. The natural setting for the analysis is instead provided by the interaction between non-trivial kinematic behaviours, induced by convective mixing, which causes stretching and folding of material elements (Childress & Gilbert 1995), and the smoothing action of diffusion. Of particular interest is therefore the analysis of flow fields which give rise to chaotic behaviour of fluid particles in the diffusionless (kinematic) limit (Aref 1984; Beigie, Leonard & Wiggins 1994; Boyland, Aref & Stremler 2000; Voth, Haller & Gollub 2002).

When diffusion is accounted for in a closed flow, fluid mixing can be described in terms of *homogenization* dynamics of the scalar field ϕ, which quantifies the relaxation towards the equilibrium state characterized by a uniform concentration throughout the mixing space. The time scales and the characteristic concentration patterns that are attained during the homogenization process are related to the eigenvalues and to the eigenfunctions of the advection–diffusion operator in the case where the flow protocol is autonomous (i.e. the velocity field $\mathbf{v}(\mathbf{x})$ does not depend on time), or of the Poincaré–Floquet operator associated with the advection–diffusion operator (which maps the concentration field over one period of flow motion) in the case of time-periodic-velocity fields $\mathbf{v}(\mathbf{x}, t + T) = \mathbf{v}(\mathbf{x}, t)$ (Giona, Cerbelli & Vitacolonna 2004*a*).

Numerical simulations (Toussaint, Carriere & Raynal 1995; Toussaint *et al.* 2000; Giona *et al.* 2004*a*; Cerbelli *et al.* 2004; Gleeson *et al.* 2004; Gleeson 2005) and theoretical analysis (Giona, Cerbelli & Vitacolonna 2004*b*; Giona *et al.* 2004*c*; Liu and Haller 2004*a*,*b*) provide a fairly detailed picture of the properties of homogenization dynamics in closed systems. We are quoting here solely those articles in which the authors solve numerically or approach analytically the advection–diffusion equation. In point of fact, there is a parallel and quantitatively consistent stream of articles which, instead of solving (1.1), analyse the *pulsed system* associated with (1.1), where the action of advection and diffusion is temporally decoupled (Sukhatme & Pierrehumbert 2002; Pikovsky & Popovich 2003). For a critical analysis of the pulsed system approximation see Giona, Adrover & Cerbelli (2005).

A detailed analysis of the dependence of homogenization time scales on the Péclet number and of the occurrence of different mixing regimes in planar flows consisting of closed streamlines is developed in Rhines & Young (1983) and Bajer, Bassom & Gilbert (2001).

For parallel autonomous flows, which is a simple class of non-chaotic flows, a theoretical prediction of the asymptotic scaling of the real part μ_R of the dominant eigenvalue of the convection-enhanced branch of the spectrum as a function of the Péclet number Pe, and of the properties of the velocity field has been obtained in Giona *et al.* (2004*b*,*c*) by enforcing the formal analogy between (1.1) and the Schrödinger equation in the presence of an imaginary potential. For the closed Couette flow, the theory predicts $-\mu_R \sim Pe^{-1/3}$ at large Pe. This result was also obtained in Thyagaraja, Loureiro & Knight (2002).

Open flow systems are ubiquitous in continuously operating flow devices (mixers, separation units, chemical reactors, laboratory equipment). As regards micromixers, typical process requirements consist of achieving a prescribed degree of mixedness at the outlet section for a segregated inlet stream. An optimal flow protocol is such that this task is accomplished within an assigned overall length of the device so as to minimize the mean residence time. The open nature of the device reflects into the boundary conditions complementing (1.1) at the inlet and outlet section, which specify the convective and/or diffusive fluxes at these boundaries of the mixing domain.

In some cases, as in the analysis of dispersion properties of solute transport in capillary and chromatographic columns (Ananthakrishnan, Gill & Barduhn 1965), the approximation of infinitely long channels may be reasonable, such as in the investigation of Taylor–Aris dispersion (Taylor 1953; Aris 1956). Specifically, in the analysis of chromatographic experiments, the focus is not centred on mixing properties of the outlet stream, but rather on the statistical distribution of the solute at the exit of the column, which can be quantified by considering the hierarchy of moments associated with the outlet concentration profile. Conversely, in all the applications in which an open flow device is used to optimize mixing performance, the finite size of the device should be enforced in the theoretical analysis of the process.

The practical design of efficient open flow devices is particularly important in MicroElectroMechanical System (MEMS) applications (Ho & Tai 1998; Squires & Quake 2005; Kim & Beskok 2007). Microfluidic applications involve microsensors, micrototal analysis systems (μTAS), microreactors for chemical and biomolecular processing (Karniandakis, Beskok & Aluru 2005; Nguyen & Wereley 2006).

The first systematic analysis of open flow devices dates back to the classical work by Danckwerts (Danckwerts 1953), which was subsequently generalized by Zwietering (Zwietering 1959). The Danckwerts' theory (Danckwerts 1953) for open flows is organized into two main contributions: (i) the definition of the residence

time distribution, which represents a global description of the flow properties of a flow device and (ii) the characterization of 'micromixing' through the use of the concepts of fluid particle age and fluid particle lifetime, based on which a cumulative index of the 'degree of micromixing' can be deduced (Danckwerts 1958). Even though residence time distributions are still used to characterize the global fluid dynamics in microdevices (Castelain *et al.* 1997; Trachsel *et al.* 2005), these quantities are generally weakly connected with the physics of mixing. In point of fact, neither the residence time distribution nor the particle-age formalism (which represents a finer characterization of the time scales associated with the survival of fluid elements within the device) provide a satisfactory measure of the mixing efficiency of an open flow system. As regards the particle-age formalism, it has been observed by several authors (see e.g. Baldyga & Bourne 1999) and references therein, that the degree of micromixing proposed by Danckwerts provides a quantitative description of the effect of back-mixing in tubular reactors but gives no information on the effect of mixing occurring within the cross-section of the equipment.

In general, open flow systems offer a variety of different operating conditions, which find no correspondence in closed devices. Moreover, in many applications (e.g. microfluidics), the Péclet number ranges in the interval $(10^1, 10^5)$, which indicates that the effect of diffusion should be necessarily taken into account (Nguyen & Wu 2005; Nguyen & Wereley 2006). Therefore, for a proper understanding of flow processes, it is essential to consider the interaction between advection and diffusion. This means that the analysis of mixing should be grounded on the study of (1.1), where advection and diffusion act alongside each other in a time continuous frame.

The analysis of mixing properties of open flow systems in the presence of diffusion is very limited, since many contributions focus on the effect of pure advection (Hardt *et al.* 2005; Metcalfe *et al.* 2006). Some authors have performed numerical investigations on the solutions of (1.1) in micromixers (Jen *et al.* 2003; Kim *et al.* 2005; Wu & Nguyen 2005). Other interesting properties of open flows have been analysed in Tel *et al.* (2005) and Straube & Pikovsky (2007). Giona, Cerbelli & Creta (2008) recently analysed the dependence of the characteristic time to reach stationary behaviour in finite-length channels.

The aim of this work is to provide a systematic analysis of the mixing properties of a simple physically realizable non-chaotic flow, obtained by the solution of the advection–diffusion equation (1.1), focusing on stationary properties. In point of fact partially chaotic or even non-chaotic flows are gaining increasing interest in microfluidics, since, due to pressure-drop and fabrication constraints, it is not always possible to achieve globally chaotic conditions (Gleeson *et al.* 2004; Nguyen & Wu 2005).

The model system considered in this article is an open Couette device, composed by coaxial cylinders of finite length, which is assumed to operate in the creeping flow regime. The process stream is pushed through the annular gap by an axial pressure drop, and is subject to the cross-sectional flow generated by the steady rotation of the cylinders, thus providing a prototypical example of helical flow. Different flow conditions can be obtained by varying the geometry (ratio between the inner to the outer cylinder radii), and the operating conditions (angular velocities of the inner and outer cylinders).

Therefore, the open Couette flow is a very versatile model for studying the occurrence of different mixing regimes, how mixing is influenced by the structure of the flow field, and what is the role of a non-uniform axial velocity profile (which is typical of open laminar flow devices) on the homogenization process.

The characterization of different mixing regimes can be approached through the spectral (eigenvalue/eigenfunction) properties of the advection–diffusion operator. We follow an approach similar to that developed in Giona *et al.* (2004*b*). Theoretical analysis is made possible by adopting the simplifying assumption of negligible axial diffusion (NAD). In § 2.4 we analyse and motivate this assumption, which is accurate starting from relatively small values of the Péclet number and of the system aspect ratio. By adopting the NAD assumption, spectral analysis simplifies to the study of a generalized second-order eigenvalue problem in the presence of an imaginary potential.

This formulation permits to unveil the occurrence of a variety of different mixing regimes which are associated with different localization properties of the convection-enhanced eigenfunctions. By changing the geometry and the angular velocities of the two cylinders several spectral 'phase-transitions' occur, which influence fluid mixing. Moreover, the behaviour of the real part of the dominant eigenvalue of the convective branch is characterized by the occurrence of a variety of different intermediate scalings. For all of these reasons, we believe that the open Couette flow may provide a useful prototype for mixing studies in laminar (non-chaotic) open mixers.

The article is organized as follows. Section 2 describes the flow model and addresses briefly the mathematical formulation of mixing in open flow systems. This section discusses also the validity of the NAD approximation. Section 3 introduces the spectral properties of the advection–diffusion operator, such as localization and spectral invariance in the case of the Couette plug flow, i.e. when axial velocity is assumed to be uniform. Section 4 addresses the spectral properties of the Couette flow and how the scaling of the dominant convection-enhanced eigenvalue depends on the geometric and flow parameters. Section 5 provides a theoretical explanation for the different scaling regimes observed, and for the localization properties of the eigenfunctions. The transition between different mixing regimes can be interpreted as a bifurcation controlled by the radius of the inner cylinder, or by the angular velocity of one of the two cylinders.

A peculiar situation occurs when the cylinders are counter-rotating. Beyond the asymptotic scaling and localization phenomena, this flow protocol admits interesting scaling regimes for intermediate values of Pe that are analysed in § 6 with the aid of several approximate methods. Finally, § 7 addresses some physically relevant observations such as the role of dimensionless numbers, and how the spectral characterization impacts on the design of finite-length devices. The appendices describe the numerical details and some analytical calculations.

2. Statement of the problem

2.1. *Flow system*

Consider the annular space between two concentric cylinders of length L_z and radii R_{in}, R_{out}, respectively (figure 1). We assume that the inner and outer cylinders rotate with constant angular speed, Ω_1 and Ω_2, respectively. An overall pressure drop $\Delta P = P_0 - P_L$ is applied to the flow device. Let (r, θ, z) be a cylindrical coordinate system coaxial with the device.

The creeping flow solution (at vanishing Reynolds numbers) of the Navier–Stokes equation for an incompressible Newtonian fluid can be obtained by superimposing the two-dimensional flow onto the cross-section $\mathbf{v}_\perp(\mathbf{x}_\perp) = (v_r(r, \theta), v_\theta(r, \theta)) = (0, v_\theta(r))$,

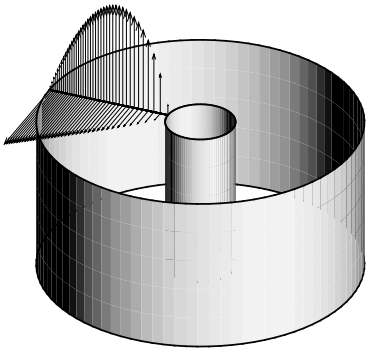

FIGURE 1. Sketch of the flow system geometry.

and the axial pressure-driven flow $v_z(r)$. The latter is given by

$$v_z(r) = \frac{\Delta P R_{out}^2}{4\mu L_z}\left[1 - \left(\frac{r}{R_{out}}\right)^2 - \frac{(1-\kappa^2)}{\log\kappa}\log\left(\frac{r}{R_{out}}\right)\right], \tag{2.1}$$

where μ is the fluid viscosity, and $R_{in} = \kappa R_{out}$, $0 < \kappa < 1$. The axial velocity vanishes at $r = R_{in}$, R_{out}. The average axial velocity over the cross-section is given by W:

$$W = \frac{\Delta P R_{out}^2}{4\mu L_z} K_f, \qquad K_f = \frac{1}{2}\left(\frac{1-\kappa^4}{1-\kappa^2} + \frac{1-\kappa^2}{\log\kappa}\right). \tag{2.2}$$

Therefore, the axial velocity can be expressed as

$$v_z(r) = \frac{W}{K_f}\left[1 - \left(\frac{r}{R_{out}}\right)^2 - \frac{(1-\kappa^2)}{\log\kappa}\log\left(\frac{r}{R_{out}}\right)\right]. \tag{2.3}$$

The cross-sectional flow $v_\theta(r)$ can be expressed as the superposition of two functions $u_h(r)$, $h = 1, 2$,

$$\frac{v_\theta(r)}{r} = \Omega_1 u_1(r) + \Omega_2 u_2(r), \tag{2.4}$$

where Ω_1, and Ω_2 are the angular velocities of the inner and outer cylinder respectively. The functions $u_h(r) = A_h + B_h/r^2$, $h = 1, 2$, subjected to the boundary conditions $u_1(R_{in}) = 1$, $u_1(R_{out}) = 0$, $u_2(R_{in}) = 0$, $u_2(R_{out}) = 1$, are given by

$$u_1(r) = \frac{1 - (R_{out}/r)^2}{1 - 1/\kappa^2}, \qquad u_2(r) = \frac{1 - (\kappa R_{out}/r)^2}{1 - \kappa^2}. \tag{2.5}$$

Let $U = \Omega_2 R_{out}$ be the velocity of the outer cylinder. The flow conditions of the system are specified by the pair of dimensionless angular velocities $\Omega = (\omega_1, \omega_2)$, where $\omega_1 = \Omega_1/\Omega_2$, and $\omega_2 = 1$. Throughout the article, we consider two flow conditions: $\Omega = (0, 1)$, corresponding to a static inner cylinder, and $\Omega = (-1, 1)$, when the inner and outer cylinder are counter-rotating with the same absolute angular speed.

In order to highlight how the spectral properties depend on the flow conditions, we consider also a simplified version of the Couette flow, corresponding to the assumption that the axial velocity is uniform across the cross-section, i.e.

$$v_z(r) = W = \text{constant}, \tag{2.6}$$

while the cross-sectional flow is still given by (2.4)–(2.5). The latter case is referred to as the Couette plug flow.

2.2. *Advection–diffusion equation*

Consider the advection–diffusion equation at steady state for the scalar field ϕ:

$$\frac{v_\theta(r)}{r}\frac{\partial\phi}{\partial\theta}+v_z(r)\frac{\partial\phi}{\partial z}=\mathscr{D}\left[\frac{1}{r}\frac{\partial}{\partial r}\left(r\frac{\partial\phi}{\partial r}\right)+\frac{1}{r^2}\frac{\partial^2\phi}{\partial\theta^2}+\frac{\partial^2\phi}{\partial z^2}\right]. \tag{2.7}$$

By introducing the dimensionless quantities

$$\rho=\frac{r}{R_{out}},\qquad \zeta=\frac{z}{L_z},\qquad w(\rho)=\frac{v_z(R_{out}\,\rho)}{W},\qquad u(\rho)=\frac{v_\theta(R_{out}\rho)}{U\rho}, \tag{2.8}$$

equation (2.7) becomes

$$\Gamma\alpha u(\rho)\frac{\partial\phi}{\partial\theta}+w(\rho)\frac{\partial\phi}{\partial\zeta}=\frac{1}{Pe}\left[\frac{\alpha^2}{\rho}\frac{\partial}{\partial\rho}\left(\rho\frac{\partial\phi}{\partial\rho}\right)+\frac{\alpha^2}{\rho^2}\frac{\partial^2\phi}{\partial\theta^2}+\frac{\partial^2\phi}{\partial\zeta^2}\right], \tag{2.9}$$

where

$$\alpha=\frac{L_z}{R_{out}},\qquad \Gamma=\frac{U}{W},\qquad Pe=\frac{WL_z}{\mathscr{D}}. \tag{2.10}$$

The geometric parameter α is the aspect ratio, and is generally much larger than 1, while Γ is the ratio of rotational to mean axial velocity. The Péclet number Pe is defined with respect to the characteristic axial velocity and to the length of channel. Other definitions of the Péclet number are possible (e.g. by considering U as a characteristic velocity and R_{out} as a characteristic length scale), which can be more useful for specific purposes (e.g. for the optimization of mixing performance). A detailed discussion of these alternative non-dimensional settings is addressed in § 7. Throughout the article we assume $\alpha=6$, $\Gamma=\pi$ (for a discussion on the influence of α and Γ see § 7). As regards the geometry of the system, we consider the two cases, $\kappa=0.4$ and $\kappa=0.8$.

Equation (2.9) is equipped with the boundary conditions $\partial\phi/\partial\rho|_{\rho=\kappa,1}=0$, expressing impermeability at the solid walls $\phi_{\theta=0}=\phi_{\theta=2\pi}$, $\partial\phi/\partial\theta|_{\theta=0}=\partial\phi/\partial\theta|_{\theta=2\pi}$, expressing the periodicity with respect to the angular variable θ and $\phi|_{\zeta=0}=\phi_{in}(\rho,\theta)$ (where ϕ_{in} is a generic inlet profile), $\partial\phi/\partial\zeta|_{\zeta=1}=0$. The latter condition at the outlet section is usually referred to as Danckwerts' boundary condition, and it can be regarded as a closure approximation necessary to specify the solution.

For high values of the Péclet number, if the aspect ratio α is significantly greater than 1, it is reasonable to neglect the axial diffusion (third term at the right-hand side of (2.9)) with respect to the cross-sectional diffusion. Therefore, (2.9) becomes

$$w(\rho)\frac{\partial\phi}{\partial\zeta}=-\Gamma\alpha u(\rho)\frac{\partial\phi}{\partial\theta}+\frac{\alpha^2}{Pe}\left[\frac{1}{\rho}\frac{\partial}{\partial\rho}\left(\rho\frac{\partial\phi}{\partial\rho}\right)+\frac{1}{\rho^2}\frac{\partial^2\phi}{\partial\theta^2}\right]. \tag{2.11}$$

Equation (2.11) is referred to as the NAD approximation associated with (2.7), and can be viewed as a parabolic advection–diffusion equation, in which the dimensionless axial coordinate ζ plays the role of time. The boundary conditions for (2.11) are the periodicity along θ, and impermeability at the inner and outer cylinders ($\zeta=\kappa$, 1), and the inlet condition $\phi|_{\zeta=0}=\phi_{in}(\rho,\theta)$ at $\zeta=0$. Since the assumption of vanishing axial diffusion reduces the order of the equation (from second to first) with respect to ζ, no boundary condition needs be specified at the outlet section. The validity of the axial diffusion approximation is discussed in § 2.4.

2.3. *Mixing in open and closed flow systems*

There are analogies and specific differences between the characterization of mixing (in the presence of diffusion) in closed and open bounded flows.

Consider first the case of a closed bounded system $\mathscr{M}$, and let $\partial_\tau \phi = -\mathbf{v}\cdot\nabla\phi + (1/Pe)\nabla^2\phi$ the dimensionless advection–diffusion equation, equipped with no-slip boundary conditions for the velocity field (supposed incompressible) at the boundary $\partial\mathscr{M}$, and with the Neumann boundary conditions $\partial\phi/\partial n|_{\partial\mathscr{M}} = 0$ for the scalar field ϕ. As discussed in § 1, mixing of a scalar concentration field in a closed system is intrinsically a time-dependent (unsteady) process which asymptotically (i.e. for $t \to \infty$) leads to a complete homogenization of the mixture, i.e. $\phi(\mathbf{x}, t) = \overline{\phi} = \text{constant}$, where $\overline{\phi} = \int_{\mathscr{M}} \phi(\mathbf{x}, 0)\, \mathrm{d}\mathbf{x}$.

Mixing efficiency is therefore expressed by the characteristic time scale at which a prescribed level of homogenization is achieved. The basic relation describing the relaxation towards the uniform state can be expressed in term of the L^2-norm of the concentration field (Cerbelli *et al.* 2004):

$$\frac{\mathrm{d}||\phi||^2_{L^2}(\tau)}{\mathrm{d}\tau} = -\frac{2||\nabla\widehat{\phi}||^2_{L^2}(\tau)}{Pe}\, ||\phi||^2_{L^2}(\tau), \tag{2.12}$$

where $\widehat{\phi} = \phi/||\phi||_{L^2}$, and

$$||\phi||_{L^2}(\tau) = \left[\int_{\mathscr{M}} |\phi(\mathbf{x}, \tau)|^2\, \mathrm{d}\mathbf{x}\right]^{1/2}, \qquad ||\nabla\widehat{\phi}||_{L^2}(\tau) = \left[\int_{\mathscr{M}} |\nabla\widehat{\phi}(\mathbf{x}, \tau)|^2\, \mathrm{d}\mathbf{x}\right]^{1/2}. \tag{2.13}$$

The characteristic homogenization time scales associated with the interplay between advection and diffusion, and the long-term properties of the system are described by the eigenvalue/eigenfunction spectrum of the advection–diffusion operator (for steady velocity fields), or of the Poincaré–Floquet operator associated with the advection–diffusion equation (for time periodic velocity fields). For further details see Cerbelli *et al.* (2004).

Turning attention to open bounded flow systems, which is the central subject of the article, the characterization and quantification of mixing efficiency is somehow more complex and involved, due to the fact that different features of the interaction between advection and diffusion are of physical and practical interest.

A general characterization of the system performance might focus on (i) transient phenomena within the flow domain $\mathscr{M}$, (ii) the relaxation dynamics towards stationary conditions in the case the inlet condition are maintained steady or (iii) the stationary response of the flow device. Point (ii) has been addressed in Giona, Cerbelli & Creta (2008) by considering the Frobenius eigenvalue associated with simple parallel flows (Schmid & Henningson 2001). The advection–diffusion equation in the presence of non-negative boundary conditions represents a typical example of a positive linear system. A linear dynamical system is said positive if, given a non-negative initial condition, the state variables of the system (here the concentration of the transported entity) remain non-negative for all positive times. For positive linear systems, a theorem due to Frobenius states that the dominant eigenvalue, i.e. the eigenvalue with the largest real part, is always real, and the corresponding eigenvector/eigenfunction can always be chosen with non-negative entries. Due to this result, the dominant eigenvalue of a positive linear system is referred to as the Frobenius eigenvalue.

In inflow–outflow systems, the Frobenius eigenvalue is tipically different from zero and quantifies the time scale to reach the steady-state profile which is not, in general a perfectly mixed state. Therefore, the Frobenius eigenvalue does not quantify mixing efficiency, but rather provides a preliminary necessary requirement to motivate the analysis of mixing efficiency at steady-state, meaning that an excessively long time

scale would suggest that a steady-state assessment of mixing efficiency might be inadequate, and that the whole transient behaviour should be considered instead.

In addressing the stationary (mixing) response of a device, which is the main subject of this article, the formalism can be simplified for channel flows where a (dimensionless) axial coordinate ζ, and a cross-section $S_\perp$ independent of ζ can be identified. For channel-like flow devices, the steady advection–diffusion equation in dimensionless form reads

$$\mathbf{v}_\perp \cdot \nabla_\perp \phi + w\, \partial_\zeta \phi = \frac{1}{Pe} \left(\nabla_\perp^2 \phi + \partial_\zeta^2 \phi \right), \tag{2.14}$$

where $\partial_\zeta \phi = \partial \phi / \partial \zeta$, $\partial_\zeta^2 \phi = \partial^2 \phi / \partial \zeta^2$, w is the axial component of the velocity field, and $\mathbf{v}_\perp$ and $\nabla_\perp$ are the cross-sectional velocity and the cross-sectional nabla operator, respectively.

Let us introduce the linear functional $\mathcal{Q}[g](\zeta)$ associated with a generic scalar function $g(\mathbf{x}_\perp, \zeta)$ defined in the mixing domain $\mathcal{M}$:

$$\mathcal{Q}[g](\zeta) = \int_{S_\perp} \left[w(\mathbf{x}_\perp, \zeta)\, g(\mathbf{x}_\perp, \zeta) - \frac{1}{Pe}\, \partial_\zeta g(\mathbf{x}_\perp, \zeta) \right] \mathrm{d}\mathbf{x}_\perp. \tag{2.15}$$

Elementary manipulations of the steady advection–diffusion equation (2.14) yield

$$\frac{\mathrm{d}}{\mathrm{d}\zeta} \mathcal{Q}[\phi](\zeta) = 0 \quad \Rightarrow \quad \mathcal{Q}[\phi](\zeta) = \text{constant}, \tag{2.16}$$

which expresses the obvious fact that at steady state the total flux (convective plus diffusive) of ϕ across any cross-section is conserved, and

$$\frac{\mathrm{d}}{\mathrm{d}\zeta} \mathcal{Q}[\phi^2](\zeta) = -\frac{2}{Pe} \int_{S_\perp} |\nabla_\perp \phi|^2 \, \mathrm{d}\mathbf{x}_\perp, \tag{2.17}$$

which is formally similar to (2.12) valid for closed system, and proves that the quantity $\mathcal{Q}[\phi^2](\zeta)$ is monotonically non-increasing with ζ.

If the NAD approximation is enforced, the functional $\mathcal{Q}[g](\zeta)$ simplifies to

$$\mathcal{Q}[g](\zeta) = \int_{S_\perp} w(\mathbf{x}_\perp, \zeta)\, g(\mathbf{x}_\perp, \zeta) \, \mathrm{d}\mathbf{x}_\perp, \tag{2.18}$$

while (2.16)–(2.17) still hold true.

Two observations follow from the structure of (2.17). If $w(\mathbf{x}_\perp, \zeta) = W = \text{constant}$, and the NAD approximation is enforced, then

$$\mathcal{Q}[\phi^2](\zeta) = W\, ||\phi||_{L^2, S_\perp} = W \int_{S_\perp} |\phi|^2 \, \mathrm{d}\mathbf{x}_\perp, \tag{2.19}$$

which implies that the stationary evolution along the axial coordinate in an tubular open flow device is formally identical to that of a closed flow system, in which the axial coordinate ζ plays the role of time, and $S_\perp$ the role of the closed mixing space $\mathcal{M}$.

On the other hand, if $w(\mathbf{x}_\perp, \zeta) \neq \text{constant}$, the steady open flow problem cannot be mapped into an equivalent closed flow system, and new features specific of open flow systems may appear, which are related to the non-uniform profile of the axial component of the velocity.

The homogenization of the cross-sectional scalar profile downstream the device axis is fully described by the spectral properties of the advection–diffusion operator. If the NAD approximation is enforced, and if the axial velocity components depend

solely on the cross-sectional coordinates $\mathbf{x}_\perp$ (as e.g. in the creeping Couette flow), (2.14) shows that the spectral problem reads

$$\lambda\, w(\mathbf{x}_\perp)\psi(\mathbf{x}_\perp) = -\mathbf{v}_\perp(\mathbf{x}_\perp)\cdot\nabla_\perp\psi(\mathbf{x}_\perp) + \frac{1}{Pe}\nabla_\perp^2\psi(\mathbf{x}_\perp), \tag{2.20}$$

where λ is the eigenvalue and $\psi(\mathbf{x}_\perp)$ the corresponding eigenfunction. Equation (2.20) is a generalized eigenvalue problem in a two-dimensional domain represented by the cross-section of the device $S_\perp$, equipped with impermeability boundary conditions $\partial\psi/\partial n|_{\partial S_\perp} = 0$, and with no-slip conditions for the cross-sectional velocity $\mathbf{v}_\perp$ on $\partial S_\perp$ ($\mathbf{v}_\perp\cdot\boldsymbol{n}|_{\partial S_\perp} = 0$, where $\boldsymbol{n}$ is the normal unit vector to $\partial S_\perp$).

2.4. *Validity of the axial-diffusion approximation*

Before addressing the spectral structure of the advection–diffusion operator, it is useful to comment on the physical validity of the NAD approximation. From what discussed in § 2.3, the axial dependence of the quantity

$$Q(\zeta) = \left[\int_{S_\perp} w(\rho)\,(\phi(\rho,\phi,\zeta) - \overline{\phi})^2\,\rho\,\mathrm{d}\rho\,\mathrm{d}\theta\right]^{1/2}, \tag{2.21}$$

where $Q(\zeta) = \mathscr{Q}[(\phi-\overline{\phi}))^2](\zeta)$, and where $\overline{\phi} = \mathscr{Q}[\phi]/\mathscr{Q}[1]$ is the (axially invariant) cross-sectional average of the scalar weighted with respect to $w(\rho)$, provides a measure of the degree of mixing along the channel, and for large Pe is a monotonically decreasing function of its argument ζ approaching zero at large ζ. Throughout this article, we consider inlet conditions such that $\overline{\phi} = 0$ and therefore $Q(\zeta)$ quantitatively coincides with $\mathscr{Q}[\phi^2](\zeta)$.

Figures 2(a) and 2(b) show the comparison of the numerical simulation of the full boundary value problem (2.9), and the results obtained by enforcing the NAD approximation, for different values of the Péclet number at $\kappa = 0.4$, and for the two different flow configurations: $\Omega = (0, 1)$ and $\Omega = (-1, 1)$. The inlet condition $\phi|_{\zeta=0} = \phi_{in}(\rho,\theta)$, as been chosen as

$$\phi_{in}(\rho,\theta) = \begin{cases} C & \text{for} \quad -\pi/2 \leqslant \theta \leqslant \pi/2 \\ -C & \text{for} \quad \pi/2 \leqslant \theta \leqslant 3\pi/2 \end{cases}, \tag{2.22}$$

where the normalization constant C is chosen such that $Q(\zeta = 0) = 1$. Figure 2(a) refers to $\Omega = (0, 1)$ i.e. to a static inner cylinder, and figure 2(b) to $\Omega = (-1, 1)$, when the inner and outer cylinders are counter-rotating. Consider figure 2(a). At $Pe = 10^2$, line (a) and (■), shows a quantitative difference between the complete equation (which includes the $1/Pe\,\partial^2\phi/\partial\zeta^2$ term) and the result of the NAD approximation can be observed, whereas starting from $Pe = 5\times10^2$, (line (b) and (○)), this difference becomes negligible and tends to zero as Pe increases further (line (c) and (●) corresponding to $Pe = 10^3$). A similar result is observed for $\Omega = (-1, 1)$ (see figure 2b). For $Pe = 2\times10^1$, (line (a) and (□)), an appreciable difference occurs between the solutions of the complete equation and the NAD approximation. As Pe increases, this difference tends to decrease (see line (b) and (■), corresponding to $Pe = 10^2$), and becomes practically negligible for $Pe \geqslant 5\times10^2$. Incidentally, figure 2(b) shows an interesting physical result, namely that the behaviour of $Q(\zeta)$ is not monotonic with Pe (the decay of $Q(\zeta)$ is faster for $Pe = 10^2$ than for $Pe = 2\times10^1$). This issue is further discussed in the remainder of the article (§§ 6 and 7).

Analogous results have been obtained for the other geometric configurations analysed ($\kappa = 0.8$), so that the value $Pe^* = 5\times10^2$ can be assumed as the lower

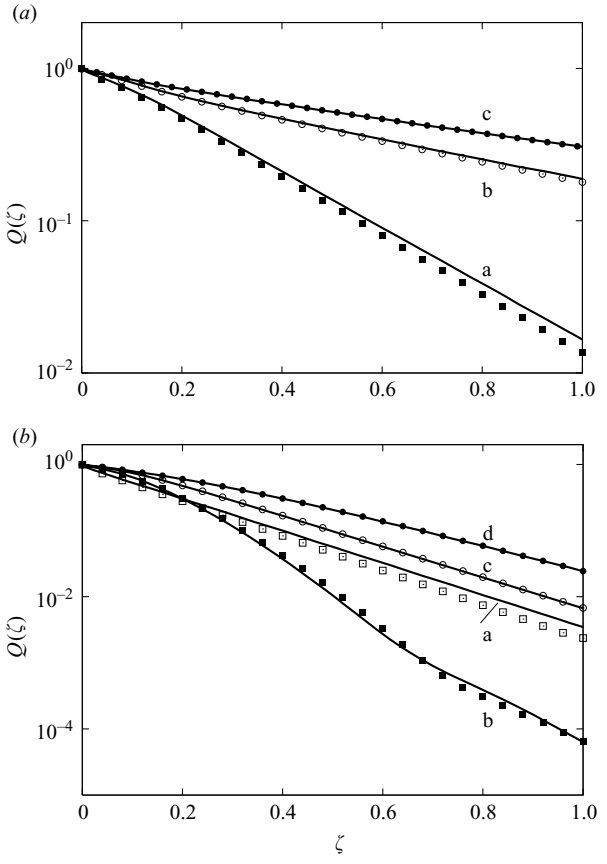

FIGURE 2. $Q(\zeta)$ versus the dimensionless axial coordinate ζ. Comparison of the complete solution (dots) and the results obtained by neglecting axial diffusion (continuous lines) for $\kappa = 0.4$, $\alpha = 6$, $\Gamma = \pi$, and for different values of the Péclet number. (*a*) $\Omega = (0, 1)$. Line (a) $Pe = 10^2$, (b) $Pe = 5 \times 10^2$, (c) $Pe = 10^3$ (NAD approximation). Dots (■): $Pe = 10^2$, (○): $Pe = 5 \times 10^2$, (●): $Pe = 10^3$ (complete solution). (*b*) $\Omega = (-1, 1)$. Line (a) $Pe = 2 \times 10^1$, (b) $Pe = 10^2$, (c) $Pe = 5 \times 10^2$, (d) $Pe = 10^3$ (NAD approximation). Dots (□): $Pe = 2 \times 10^1$, (■): $Pe = 10^2$, (○): $Pe = 5 \times 10^2$, (●): $Pe = 10^3$ (complete solution).

threshold starting from which the NAD approximation is reliable for the current values $\alpha = 6$ and $\Gamma = \pi$ of the aspect and velocity ratio, respectively.

2.5. *Localization: a first phenomenological view*

In order to motivate spectral analysis of the advection–diffusion operator that is developed in this article, let us first consider a simple mixing experiment. Consider the Couette system at $\kappa = 0.4$, $\Omega = (-1, 1)$ and $Pe = 10^6$, starting from the inlet condition (2.22). As for static mixers (Hobbs & Muzzio 1998; Szalai & Muzzio 2003), one can consider the device resulting from connecting in series several identical mixing units, and analyse the partially mixer structures in stationary conditions at the outlet section of each unit. Figure 3 show the contour plot of the concentration profiles (normalized to unit square integral norm weighted with respect to the axial velocity), and the end of the second and the fifth unit, and the concentration profiles in the corresponding outlet sections evaluated at $\theta = \pi/2$. As can be observed, the

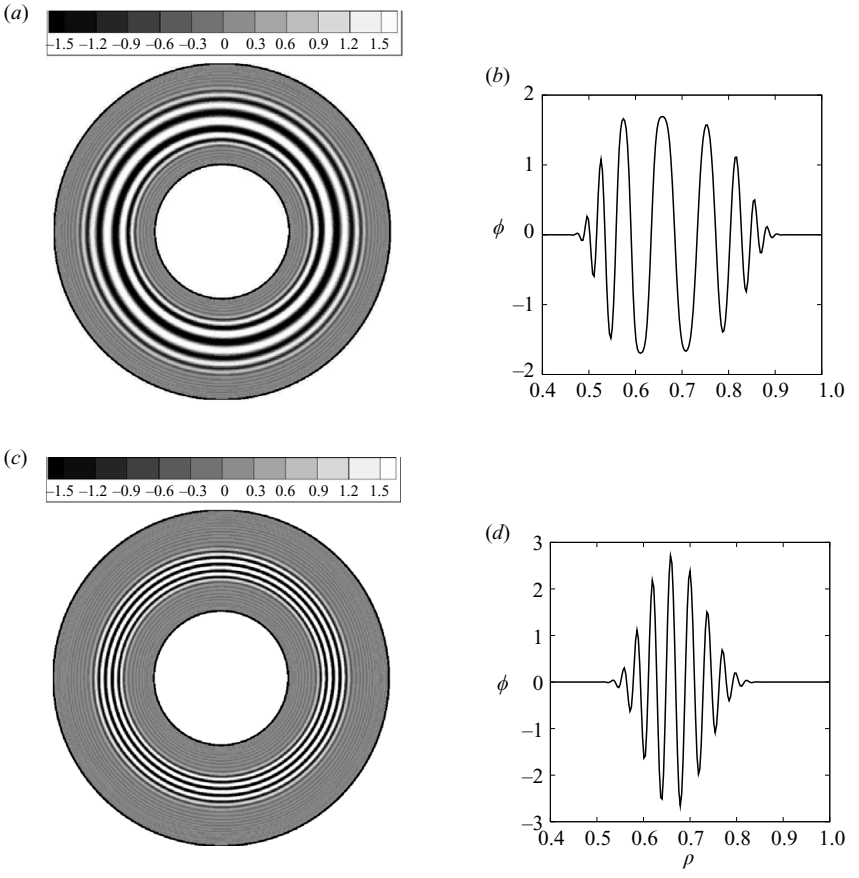

FIGURE 3. Contour plots of the concentration profiles at the outlet sections of a mixer consisting of several $n = 1, 2, \ldots$ Couette units. (a) $n = 2$, (c) $n = 5$. (b), (d) Concentration profiles at $\theta = \pi/2$ at the outlet section of the second and fifth units. In the contour plots black and white regions correspond to high negative and positive values of the concentration, respectively, grey regions to vanishing values of ϕ.

partially mixed structures become progressively localized at some internal point of the cross-section, showing a rather complex lamellar structure.

The localization of the concentration pattern is a typical feature of the interplay between advection and diffusion in open flow systems, which determines the occurrence of different mixing regimes associated with different scalings of the homogenization exponent with the Péclet number. This phenomenon controls the whole mixing process and sets in also in the early stage of the homogenization process. With reference to figure 3 the values of the normalized variance $Q(\zeta)$ (i.e. such that $Q(0) = 1$) at the outlet sections of the second and fifth modulus are $Q = 0.57$, and $Q = 0.15$ respectively.

For a device composed by a sufficiently large number of Couette units, attains an almost invariant shape. In the case of the operating conditions, depicted in figure 3, this occurs starting from the tenth modulus (not shown for the sake of brevity). The occurrence of invariant structures in the concentration profiles are controlled by the eigenfunctions of the advection–diffusion operator. This motivates the analysis of the spectral (eigenvalues/eigenfunctions) structure of this operator developed in the remainder of the article.

There is another relevant piece of information associated with the concentration profiles depicted in figure 3. The localized patterns shown in figure 3 suggest that the chosen inlet condition excites the eigenfunctions of the advection–diffusion operator associated with the convection-enhanced branch of the spectrum (Giona *et al.* 2004*b*,*c*), since the eigenfunctions associated with the diffusive branches are not localized but global functions.

Indeed, in the case of simple flows such as the open Couette system, the eigenfunctions of the convection enhanced branch are particularly interesting, since they are associated with a significant enhancement in homogenization process. All of these issues (localization, structure and scaling of the convection-enhanced spectral branches) are addressed in the following paragraphs.

3. Dominant eigenvalue and eigenfunction localization

Let us consider the advection–diffusion equation for $Pe \geqslant Pe^*$, $Pe^* \simeq 5 \times 10^2$, i.e. in the range where the NAD approximation provides a reliable description of the interplay between advection and diffusion.

Since the cross-sectional velocity depends exclusively on ρ, it is convenient to expand the solution of (2.11) with respect to the $\mathrm{e}^{-im\theta}$, $m \in \mathbb{Z}$, $i = \sqrt{-1}$:

$$\phi(\zeta, \rho, \theta) = \sum_{m=-\infty}^{\infty} \phi_m(\zeta, \rho)\, \mathrm{e}^{-im\theta} \tag{3.1}$$

to obtain for the Fourier coefficients $\phi_m(\zeta, \rho)$ the system of equations

$$w(\rho)\, \frac{\partial \phi_m}{\partial \zeta} = im\Gamma\alpha u(\rho)\, \phi_m + \varepsilon_\alpha \left[\frac{1}{\rho}\, \frac{\partial}{\partial \rho} \left(\rho\, \frac{\partial \phi_m}{\partial \rho} \right) - \frac{m^2}{\rho^2}\, \phi_m \right], \qquad m \in \mathbb{Z}, \tag{3.2}$$

where $\varepsilon_\alpha = \alpha^2/Pe$. Equation (3.2) shows that the solution of (2.11) decouples into a countable family of one-dimensional parabolic problems which depend on the radial coordinate ρ and are parametrized with respect to m. Henceforth, the spectral properties of the advection–diffusion operator associated with (3.2) are addressed.

3.1. *Norm conditions and eigenvalues*

This section derives some basic equalities for the real, μ, and imaginary, q, part of the eigenvalues $\lambda = \mu + iq$ as a function of the norms and linear functionals of the corresponding eigenfunction ψ. The eigenvalue problem associated with (3.2) can be rewritten in a compact form as

$$\lambda\, w(\rho)\, \psi(\rho) = \varepsilon_\alpha\, \mathscr{D}_2[\psi](\rho) + i\, V(\rho)\, \psi(\rho), \tag{3.3}$$

where $V(\rho) = m\Gamma\alpha\, u(\rho)$ and

$$\mathscr{D}_2[\psi](\rho) = \frac{1}{\rho}\, \frac{\mathrm{d}}{\mathrm{d}\rho} \left(\rho\, \frac{\mathrm{d}\psi(\rho)}{\mathrm{d}\rho} \right) - \frac{m^2}{\rho^2}\, \psi(\rho). \tag{3.4}$$

For $m = 0$, $V(\rho) = 0$ identically, and (3.4) reduces to $\lambda\, w(\rho)\, \psi(\rho) = \varepsilon_\alpha \mathscr{D}_2[\psi](\rho)$, in which solely the action of diffusion contributes to mixing. Since the contribution of cross-sectional convection is immaterial, the set of eigenvalues associated with the eigenvalue problem are referred to as *diffusive* component of the spectrum. It can be straightforwardly seen that the real part eigenvalue of the diffusive spectral component, is directly proportional to the inverse of the Péclet number, i.e. $-\mu_{diff} \sim 1/Pe$. The diffusive eigenfunctions do not depend on θ. Their level

curves coincide with the streamlines of the flow, and this is the reason why advection does not contribute to mixing.

For $m \neq 0$, the interplay between advection and diffusion becomes effective, and the corresponding systems of eigenvalues/eigenfunctions is referred to as the *convection-enhanced* spectral component. The dominant eigenvalue of this component is generally obtained by setting $m = 1$. In point of fact, in the case where $\Omega = (-1, 1)$, there is a small interval of Pe values in which the eigenvalue with the smallest (in absolute value) real part of the $(m = 2)$ system becomes slightly smaller than the eigenvalues of the $(m = 1)$ system. This issue is briefly addressed in § 4.1.

A generic inlet condition possesses non-vanishing projection on the diffusive eigenfunctions of the spectrum. However, by exploiting the symmetries of the system, it is possible to avoid this part, by choosing inlet conditions that possess vanishing projections onto the diffusive branch. This is the case of the inlet condition expressed by (2.22), and more generally of any inlet profile that does not depend on the radial coordinate. For any choice of this type of inlet profile, mixing performance is controlled by the convection-enhanced part of the spectrum, the dependence of which on the Péclet number is all but trivial.

However, the diffusive spectral component (occurring for $m = 0$) plays a role in other physical phenomena that are not strictly related to homogenization. For $m = 0$, the cross-sectional velocity component does not contribute to homogenization, and thus the resulting spectral structures derive solely from the interaction between the axial velocity and cross-sectional diffusion. These spectral structures play a significant role in the analysis of dispersion phenomena at high Péclet number (Giona, Adrover & Cerbelli 2009) and in the study of mixing layers in microdevices and T-junctions (Salmon & Ajdari 2007).

In approaching stationary homogenization properties, the characterization of the spectral structures (eigenvalues/eigenfunctions) of the operator (3.3) provides a way of obtaining the asymptotic patterns controlling the homogenization process and the scaling of the corresponding homogenization exponents, which are related to the real part of the eigenvalues. The tools for characterizing the spectral behaviour are essentially two: (i) the observation that the convection-enhanced spectral components give rise to localized eigenfunctions for high Péclet number, and (ii) the use of simple integral (norm) equalities, which are described below, in order to predict the behaviour of the real part of the eigenvalues as a function of the local structure of the axial and cross-sectional velocities near the localization point. This approach is similar to that applied for simple closed flows in Giona *et al.* (2004*b*,*c*), and can be viewed as a form of boundary-layer theory, in which the boundary layer corresponds to the localized eigenstructures, and the norm equalities provide a tool for quantifying both the width of the boundary layer and the homogenization rates.

Let $L^2_\rho([\kappa, 1])$ the space of square summable functions in the interval $(\kappa, 1)$, equipped with the inner product $\langle \phi, \psi \rangle = \int_\kappa^1 \rho\, \phi(\rho)\, \psi^*(\rho)\, \mathrm{d}\rho$, where ψ^* is the complex conjugate of ψ. By taking the inner product of (3.3) with respect to a constant real-valued function, and observing that $\langle \mathscr{D}_2[\psi], 1 \rangle = 0$, and that both $w(\rho)$ and $V(\rho)$ are real-valued functions, one obtains $\lambda \langle w\, \psi, 1 \rangle = \lambda \langle \psi, w \rangle = i\, \langle V\, \psi, 1 \rangle = i\, \langle \psi, V \rangle$, and therefore

$$\lambda\, \langle \psi, w \rangle = i\, \langle \psi, V \rangle. \tag{3.5}$$

A second useful equality relating the eigenvalues to the norms of the corresponding eigenfunctions can be obtained by taking the inner product of (3.3) with the eigenfunction $\psi(\rho)$ itself.

Due to the boundary conditions of Neumann type on ψ, one obtains

$$\int_\kappa^1 \frac{\mathrm{d}}{\mathrm{d}\rho}\left(\rho\,\frac{\mathrm{d}\psi}{\mathrm{d}\rho}\right)\psi^*(\rho)\,\mathrm{d}\rho = -\int_\kappa^1 \rho\left|\frac{\mathrm{d}\psi}{\mathrm{d}\rho}\right|^2 \mathrm{d}\rho = -||\partial_\rho\psi||_{L^2}^2, \tag{3.6}$$

where $||\psi||_{L^2}^2 = \langle\psi, \psi\rangle$. Therefore, the inner product of (3.3) with ψ leads to

$$\lambda\,||\psi||_w^2 = -\varepsilon_\alpha\left[||\partial_\rho\psi||_{L^2}^2 + m^2\,||\psi/\rho\,||_{L^2}^2\right] + i\,\langle V\,\psi, \psi\rangle, \tag{3.7}$$

where $||\psi||_w^2 = \langle w\,\psi, \psi\rangle$. Since $\langle V\,\psi, \psi\rangle \in \mathbb{R}$, (3.7) can be decomposed into two separate equations for the real (μ) and the imaginary (q) part of the eigenvalues

$$\mu = -\frac{\varepsilon_\alpha}{||\psi||_w^2}\left[||\partial_\rho\psi||_{L^2}^2 + m^2\,||\psi/\rho\,||_{L^2}^2\right] \tag{3.8}$$

and

$$q = \frac{\langle V\,\psi, \psi\rangle}{||\psi||_w^2}. \tag{3.9}$$

It can be observed that (3.5) and (3.7) can be envisioned as deriving from the generic weak formulation of the eigenvalue problem, $\lambda\langle w\psi, f\rangle = -\varepsilon_\alpha\langle\partial_\rho\psi, \partial_\rho f\rangle + i\langle V\,\psi, f\rangle$, whereupon f is chosen equal to 1 or ψ. Equation (3.9) indicates that the real part of the eigenvalues is always non-positive, and that, for $m \neq 0$, i.e. for the eigenvalues of the convection-enhanced component, is strictly negative. This result is a direct consequence of the dissipative nature of the advection–diffusion equation. Equations (3.5), (3.8)–(3.9) are extensively used in the remainder of the article to derive explicitly the dependence of the dominant eigenvalue (of the convection-enhanced spectral branch) on the Péclet number.

3.2. *The case of the Couette plug flow*

Before addressing the spectral structure of the advection–diffusion operator for the Couette flow, it is useful to analyse the properties of the Couette plug flow, which is obtained by setting $w(\rho) = 1$.

The spectral properties of the advection–diffusion operator in stationary conditions for the Couette plug flow are identical to those of a two-dimensional closed Couette flow defined on $S_\perp$, and have been briefly addressed in Giona *et al.* (2004*b*).

Consider $m = 1$, i.e. the spectral system possessing the dominant convection-enhanced eigenvalue. Figure 4 shows the spectrum of the advection–diffusion operator for $m = 1$ ($\alpha = 6$, $\Gamma = \pi$) for $\kappa = 0.4$ (figure 4*a*,*b*) and for $\kappa = 0.8$ (figure 4*c*,*d*), for several values of the Péclet number (see Appendix A for details on the numerical solution of the eigenvalue problem). Figures 4(*a*, *b*) and 4(*c*, *d*) refer to the operating conditions $\Omega = (0, 1)$, and $\Omega = (-1, 1)$, respectively.

The convection-enhanced branches of the Couette plug flow are characterized by *spectral invariance*: as Pe increases the eigenvalues lie on a single master curve, as can be observed from figure 4(*a*–*d*). This phenomenon has been observed for different non-chaotic closed flow systems (Giona *et al.* 2004*b*).

Let $-\mu_d$ be the real part with reversed sign (μ_d is negative by (3.8)) of the dominant eigenvalue of the convection-enhanced branch, and $\psi_d(\rho) = \psi_d^R + i\psi_d^I$ the corresponding eigenfunction. The scaling of $-\mu_d$ as a function of Pe is depicted in figure 5. Independently of κ and Ω, and for sufficiently large ($Pe \geqslant 10^4$) μ_d is characterized by the scaling

$$-\mu_d \sim Pe^{-1/3} \sim \varepsilon_\alpha^{1/3}. \tag{3.10}$$

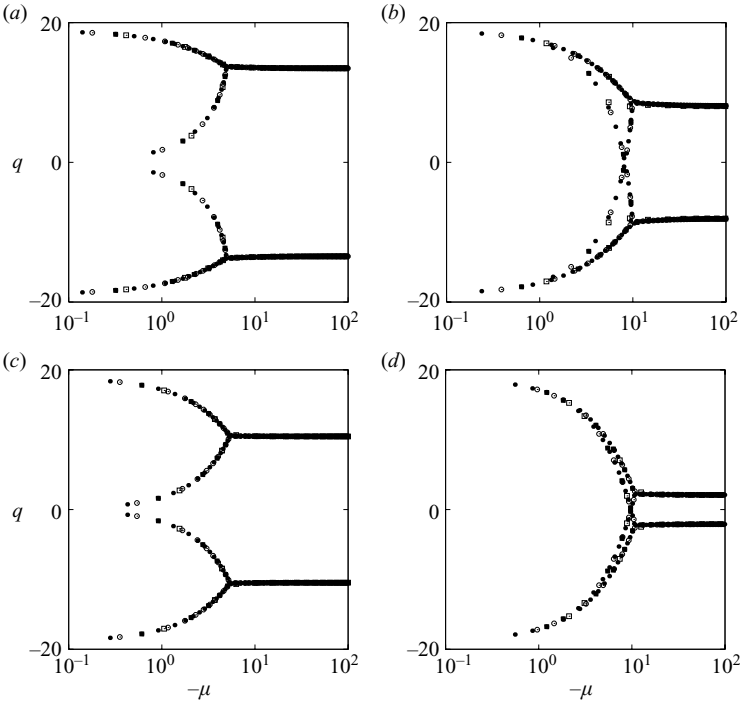

FIGURE 4. Spectrum of the ($m=1$) convective branch of the Couette plug flow ($\alpha=6$, $\Gamma=\pi$). (a) $\kappa=0.4$, $\Omega=(0,1)$. (□): $Pe=5\times10^3$, (■): $Pe=10^4$, (○): $Pe=5\times10^4$, (●): $Pe=10^5$. (b) $\kappa=0.4$, $\Omega=(-1,1)$. (□): $Pe=10^3$, (■): $Pe=5\times10^3$, (○): $Pe=2\times10^4$, (●): $Pe=8\times10^4$. (c) $\kappa=0.8$, $\Omega=(0,1)$. (□): $Pe=2\times10^4$, (■): $Pe=10^5$, (○): $Pe=5\times10^5$, (●): $Pe=10^6$. (d) $\kappa=0.8$, $\Omega=(-1,1)$. (□): $Pe=10^4$, (■): $Pe=5\times10^4$, (○): $Pe=10^5$, (●): $Pe=5\times10^5$.

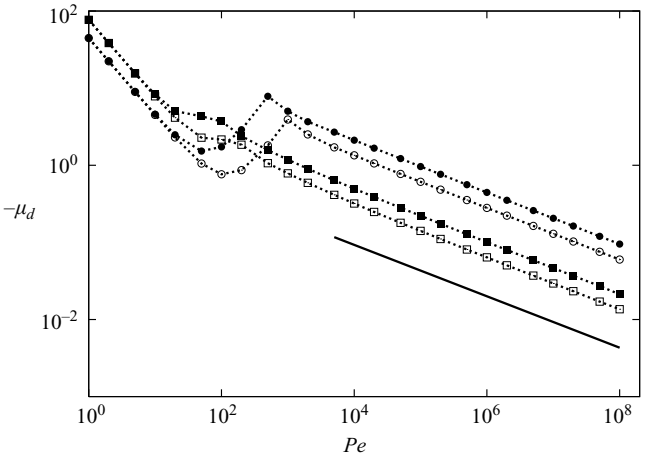

FIGURE 5. Real part of the eigenvalue μ_d of the convection-enhanced branch versus Pe for the Couette plug flow ($\alpha=6$, $\Gamma=\pi$). Symbols (●) refer to $\kappa=0.8$, $\Omega=(-1,1)$, (○) to $\kappa=0.8$, $\Omega=(0,1)$, (■) to $\kappa=0.4$, $\Omega=(-1,1)$, (□) to $\kappa=0.4$, $\Omega=(0,1)$. The solid line depicts the scaling $\mu\sim Pe^{-1/3}$.

There is another peculiarity that can be observed from the data depicted in figure 5, namely the occurrence of a non-monotonic behaviour of the dominant eigenvalue at increasing Pe. Specifically, while for $\kappa=0.4$ the real part $-\mu_d$ is a monotonically

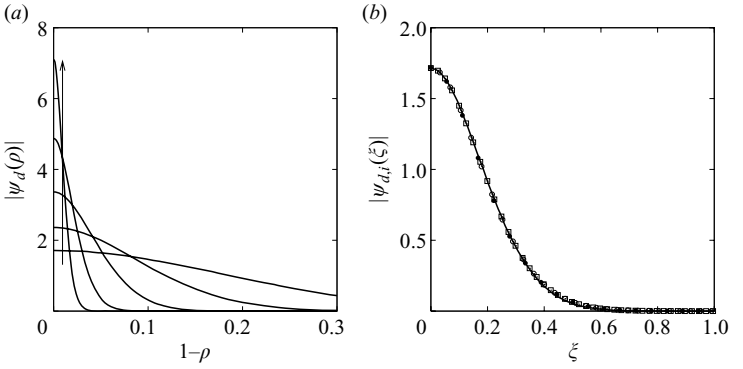

FIGURE 6. (*a*) Modulus of the dominant eigenfunction $|\psi_d(\rho)|$ of the convective branch versus $1-\rho$ for the Couette plug flow with $\kappa=0.4$, $\Omega=(-1,1)$. The arrow indicates increasing values of $Pe=10^3,\ 10^4,\ 10^5,\ 10^6,\ 10^7$. (*b*) Invariant rescaling of of the dominant eigenfunction $|\psi_i(\xi)|$ of the convective branch versus $\xi=(1-\rho)/\beta(\varepsilon)$ for the Couette plug flow at $\kappa=0.4$, $\Omega=(-1,1)$. Solid line corresponds to $Pe=10^4$, dots (□) to $Pe=10^5$, (○) to $Pe=10^6$, (●) to $Pe=10^7$.

decreasing function of Pe, for $\kappa=0.8$ the graph of $-\mu_d(Pe)$ displays a local maximum occurring for $Pe\simeq(10^3,\ 2\times10^3)$, depending on the operating conditions. This means that there exist intermediate values of the Péclet number for which mixing performance is optimal. This phenomenon is even more pronounced for the creeping Couette flow and is addressed in § 6.

The scaling law equation (3.10) is a consequence of the localization of the dominant convective eigenfunction close to the walls of the flow domain (there exist spectral branches that become localized close to $\rho=\kappa$ and close to $\rho=1$, but the branch possessing the lowest decay exponent corresponds to eigenfunctions localized at $\rho=1$). Eigenfunction localization becomes more pronounced as Pe increases. This phenomenon is depicted in figure 6(*a*), for $\kappa=0.4$, $\Omega=(-1,1)$.

In point of fact, for Pe large enough, the dominant eigenfunctions $\psi_d(\rho;\varepsilon_\alpha)$ (the explicit dependence of ψ_d on the parameter ε_α is here included) admits an invariant rescaling

$$\psi_d(\rho;\varepsilon_\alpha)=A(\varepsilon_\alpha)\,\psi_{d,i}\left(\frac{1-\rho}{\beta(\varepsilon_\alpha)}\right),\qquad \varepsilon_\alpha\to0, \tag{3.11}$$

where $\psi_{d,i}$ is an invariant function independent of Pe, i.e. of ε_α, $\beta(\varepsilon_\alpha)\to0$ for $\varepsilon_\alpha\to0$, and $A(\varepsilon_\alpha)$ is a normalization factor (such that the eigenfunction norm equals 1). The occurrence of the invariant rescaling expressed by (3.11) is depicted in figure 6(*b*) for $\kappa=0.4$, $\Omega=(-1,1)$. Analogous results are obtained for any other operating conditions of the Couette plug flow.

3.3. *Scaling of the dominant convective eigenvalue*

Although the analysis developed in Giona *et al.* (2004*b*) permits to predict the scaling behaviour (3.10) found for the Couette plug flow, the derivation of this equation in a cylindrical system has not been reported elsewhere. For this reason, this section briefly addresses these properties, since the method adopted for the Couette plug flow can be adapted with minor modifications to the more complex cases of the creeping Couette flow, i.e. when $w(\rho)$ is no longer constant.

Essentially, in order to predict the asymptotic scaling of the dominant convective eigenfunction, two main results are needed: (i) the equalities expressed by (3.8) and

(3.5), and (ii) the *localization ansatz* and the resulting invariant rescaling expressed by (3.11). The proof of (3.10) follows by enforcing (3.11) within (3.7) and (3.5).

Let us assume the validity of (3.11), where $\beta(\varepsilon_\alpha)$ is an unknown function of ε_α, which is solely characterized by the property of being a monotonically decreasing function of its argument, tending to zero for $\varepsilon_\alpha \to 0$ (this follows from the localization ansatz).

Substituting (3.11) into the expression for the L^2-norm of ψ_d,

$$||\psi_d||^2_{L^2} = A^2(\varepsilon_\alpha) \int_\kappa^1 \left| \psi_{d,i}\left(\frac{1-\rho}{\beta(\varepsilon_\alpha)}\right)\right|^2 \rho \, \mathrm{d}\rho, \tag{3.12}$$

and making the change of variable $1-\rho = \xi\,\beta(\varepsilon_\alpha)$, the integration limits become $\xi_1 = 0$ (for $\rho = 1$), and $\xi_2 = (1-\kappa)/\beta(\varepsilon_\alpha)$ (for $\rho = \kappa$). For small ε_α, $\xi_2 \gg 1$, and since the function $\psi_{d,i}$ is localized in a neighbourhood of $\xi = 0$, the upper integration limit can be substituted with $\xi_2 = \infty$. Therefore, (3.12) becomes

$$\begin{aligned} ||\psi_d||^2_{L^2} &= A^2(\varepsilon_\alpha)\,\beta(\varepsilon_\alpha) \int_0^\infty |\psi_{d,i}(\xi)|^2 (1-\xi\beta(\varepsilon_\alpha))\,\mathrm{d}\xi = A^2(\varepsilon_\alpha)\,\beta(\varepsilon_\alpha)\,[C_0 - \beta(\varepsilon_\alpha) C_1] \\ &= A^2(\varepsilon_\alpha)\,\beta(\varepsilon_\alpha)\,C_0 + O(\beta^2), \end{aligned} \tag{3.13}$$

where $C_0 = \int_0^\infty |\psi_{d,i}(\xi)|^2\,\mathrm{d}\xi$ and $C_1 = \int_0^\infty \xi\,|\psi_{d,i}(\xi)|^2\,\mathrm{d}\xi$.

In a similar way, the remaining norms entering (3.8) can be expressed as

$$\begin{aligned} ||\psi_d/\rho||^2_{L^2} &= A^2(\varepsilon_\alpha) \int_\kappa^1 \frac{1}{\rho} \left| \psi_{d,i}\left(\frac{1-\rho}{\beta(\varepsilon_\alpha)}\right)\right|^2 \mathrm{d}\rho = A^2(\varepsilon_\alpha)\,\beta(\varepsilon_\alpha) \int_0^\infty \frac{|\psi_{d,i}(\xi)|^2}{1-\xi\beta(\varepsilon_\alpha)}\,\mathrm{d}\xi \\ &= A^2(\varepsilon_\alpha)\,\beta(\varepsilon_\alpha)\,C_0 + O(\beta^2), \end{aligned} \tag{3.14}$$

and

$$\begin{aligned} ||\partial_\rho \psi_d||^2_{L^2} &= A(\varepsilon_\alpha) \int_\kappa^1 \rho \left| \frac{\partial \psi_{d,i}((1-\rho)/\beta(\varepsilon_\alpha))|^2}{\partial \rho}\right|^2 \mathrm{d}\rho = \frac{A^2(\varepsilon_\alpha)}{\beta(\varepsilon_\alpha)}\,[D_0 + \beta(\varepsilon_\alpha) D_1] \\ &= \frac{A^2(\varepsilon_\alpha)}{\beta(\varepsilon_\alpha)} D_0 + O(1), \end{aligned} \tag{3.15}$$

where $D_0 = \int_0^\infty |\partial\psi_{d,i}(\xi)\partial\xi|^2\,\mathrm{d}\xi$, $D_1 = \int_0^\infty \xi\,|\partial\psi_{d,i}(\xi)\partial\xi|^2\,\mathrm{d}\xi$. By substituting (3.13)–(3.15) into (3.8), the real part of the dominant convective eigenvalue of the Couette plug flow can be expressed as

$$-\mu_d = \varepsilon_\alpha \left[\frac{D_0}{\beta^2(\varepsilon_\alpha)\,C_0} + O(1)\right], \tag{3.16}$$

and therefore for small ε_α

$$-\mu_d = \frac{\varepsilon_\alpha}{\beta^2(\varepsilon_\alpha)}\,K_0 + O(\varepsilon_\alpha), \tag{3.17}$$

where $K_0 = D_0/C_0$.

Let us now consider (3.5), which in the plug flow case simplifies to $\lambda_d\,\langle \psi_d, 1\rangle = i\,\langle \psi_d, V\rangle$. Since the dominant convection-enhanced eigenfunctions become progressively localized at $\rho = 1$ at increasing Péclet number, solely the behaviour of the potential $V(\rho)$ near the wall $\rho = 1$ influences the scaling of the dominant convective eigenvalue. Near $\rho = 1$ one can expand $V(\rho)$ as

$$V(\rho) = V_0 + V_1(1-\rho) + O(|1-\rho|^2). \tag{3.18}$$

Substituting the invariant rescaling (3.11), and making use of (3.18) up to leading (first) order, the two integrals entering (3.5) can be expressed as

$$\begin{aligned}\langle \psi_d, 1\rangle &= A(\varepsilon_\alpha)\,\beta(\varepsilon_\alpha)\int_0^\infty (1-\beta(\varepsilon_\alpha)\,\xi)\,\psi_{d,i}(\xi)\,\mathrm{d}\xi \\ &= A(\varepsilon_\alpha)\,\beta(\varepsilon_\alpha)\,[G^0-\beta(\varepsilon_\alpha)\,G^1], \qquad (3.19)\\ \langle \psi_d, V\rangle &= A(\varepsilon_\alpha)\,\beta(\varepsilon_\alpha)\int_0^\infty [1-\beta(\varepsilon_\alpha)\,\xi]\;[V_0+V_1\,\beta(\varepsilon_\alpha)\,\xi)]\;\mathrm{d}\xi \\ &= A(\varepsilon_\alpha)\,\beta(\varepsilon_\alpha)\,\left[V_0\,G_0+\beta(\varepsilon_\alpha)\,(V_1-V_0)\,G^1-\beta^2(\varepsilon_\alpha)\,V_1\,G^2\right], \qquad (3.20)\end{aligned}$$

where

$$G^h=\int_0^\infty \xi^h\,\psi_{d,i}(\xi)\,\mathrm{d}\xi = G^h_R + i\,G^h_I\,, \qquad h=0,1,2. \qquad (3.21)$$

The decomposition into real and imaginary parts of the dominant eigenvalue in (3.5), leads to a linear system for μ_d and q_d

$$\begin{pmatrix} G^0_R-\beta\,G^1_R & -G^0_R+\beta G^1_I \\ G^0_R-\beta G^1_I & G^0_R-\beta\,G^1_R \end{pmatrix}\begin{pmatrix}\mu_d\\ q_d\end{pmatrix}=\begin{pmatrix} -V_0G^0_I-\beta(V_1-V_0)G^1_I-V_1G^0_I+\beta^2V_1G^2_I \\ V_0G^0_R+\beta(V_1-V_0)G^1_R+V_1G^0_I-\beta^2V_1G^2_R\end{pmatrix} \qquad (3.22)$$

that yields for $-\mu_d$:

$$-\mu_d=\beta(\varepsilon_\alpha)\,\frac{V_1\left(G^0_R\,G^1_I-G^0_I\,G^1_R\right)}{\left(G^0_R\right)^2+\left(G^0_I\right)^2}+O(\beta^2(\varepsilon_\alpha))=\beta(\varepsilon_\alpha)K_1+O(\beta^2(\varepsilon_\alpha)). \qquad (3.23)$$

Equating (3.17) and (3.23) up to the leading order, one obtains for large Pe (small ε_α)

$$\frac{\varepsilon_\alpha K_0}{\beta^2(\varepsilon_\alpha)}=\beta(\varepsilon_\alpha)K_1 \Rightarrow \beta^3(\varepsilon_\alpha)=\varepsilon_\alpha\left(\frac{K_0}{K_1}\right), \qquad (3.24)$$

i.e.

$$\beta(\varepsilon_\alpha)=\overline{K}\,\varepsilon_\alpha^{1/3}, \qquad (3.25)$$

where $\overline{K}=(K_0/K_1)^{1/3}$, which, from (3.18), implies for sufficiently large Pe

$$-\mu_d=\frac{K_0}{\overline{K}^2}\,\varepsilon_\alpha^{1/3}\sim Pe^{-1/3}. \qquad (3.26)$$

Equation (3.26) corresponds to the scaling observed numerically for the real part of the dominant convection-enhanced eigenvalue of the Couette plug flow (see figure 5).

4. Advection–diffusion in the creeping Couette flow

This section describes the spectral phenomenology associated with the advection–diffusion equation for the open Couette flow under creeping conditions, by assuming the NAD approximation. From the physical point of view, the spectral results obtained by enforcing NAD approximation are significant solely starting from $Pe > Pe^*$, where $Pe^* \simeq 5\times 10^2$, as discussed in § 2.4.

The main difference with respect to the Couette plug flow considered in § 3, modelling transient mixing in an annular domain, is the presence of a non-uniform axial velocity profile $w(\rho)$, which vanishes at the solid walls (inner and outer cylinders). The non-uniform character of the axial velocity profile makes it impossible to

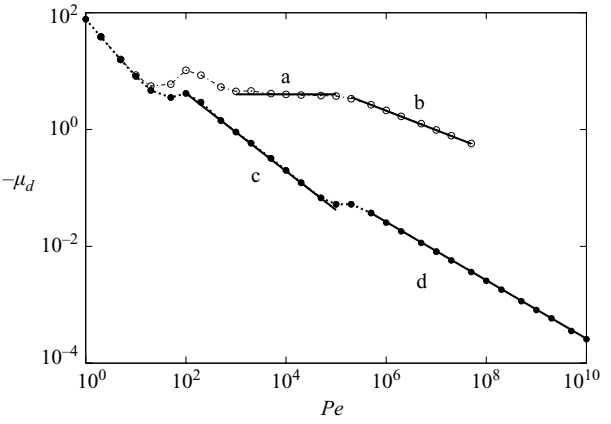

FIGURE 7. Real part of the dominant convection-enhanced eigenvalue μ_d versus Pe for the Couette flow $\kappa = 0.4$, $\alpha = 6$, $\Gamma = \pi$. Upper curve (and symbols ○) refer to $\Omega = (-1, 1)$, lower curve (and symbols ●) to $\Omega = (0, 1)$. Solid line (a) corresponds to the scaling $-\mu_d \sim$ constant, solid line (b) to $\mu_d \sim Pe^{-1/3}$, solid line (c) to $-\mu_d \sim Pe^{-2/3}$, solid line (d) to the scaling $-\mu_d \sim Pe^{-1/2}$.

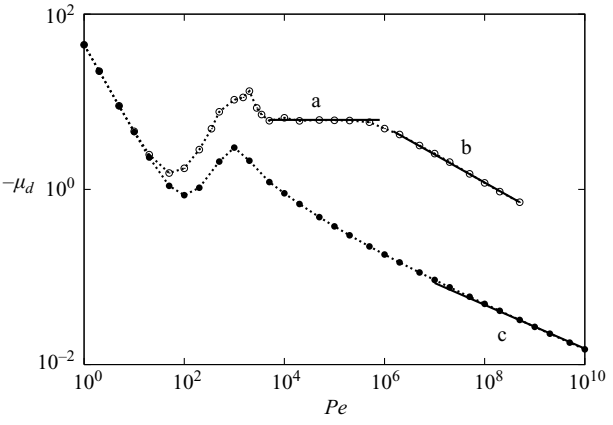

FIGURE 8. Real part of the dominant convection-enhanced eigenvalue μ_d versus Pe for the Couette flow $\kappa = 0.8$, $\alpha = 6$, $\Gamma = \pi$. Upper curve (and symbols ○) refer to $\Omega = (-1, 1)$, lower curve (and symbols ●) to $\Omega = (0, 1)$. Solid line (a) corresponds to the scaling $-\mu_d \sim$ constant, solid line (b) to $-\mu_d \sim Pe^{-1/3}$, solid line (c) to $-\mu_d \sim Pe^{-1/4}$.

transform the stationary advection–diffusion equation for an open flow device into an equivalent problem for a closed system.

Next, we show that the presence of a non-uniform axial velocity determines an extremely rich spectral behaviour of the advection–diffusion operator that has no counterpart in the corresponding closed flow system.

4.1. *Asymptotic spectral regimes*

Figures 7 and 8 review the behaviour of μ_d for different geometric and operating configurations ($\kappa = 0.4$, figure 7 and $\kappa = 0.8$, figure 8, respectively). For almost all the Péclet values, the dominant eigenvalue of the convection-enhanced spectral component corresponds to $m = 1$ in (A 10).

κ	Ω	γ
0.4	(0, 1)	1/2
0.4	(−1, 1)	1/3
0.8	(0, 1)	1/4
0.8	(−1, 1)	1/3

TABLE 1. Asymptotic scaling exponent γ entering (4.1) for the different geometric and operating conditions considered throughout this article.

This is true for all the Couette flow systems considered with the unique exception of the case $\kappa = 0.8$, $\Omega = (-1, 1)$. For this flow condition, there is a small window of Péclet values, $Pe \in (1885, 2000)$, for which the dominant eigenvalue of the convection-enhanced component corresponds to $m = 2$. However, the difference between the real parts of the dominant eigenvalues of the $(m = 1)$ and $(m = 2)$ branches within this window of Pe values is very small. The maximal difference occurs for $Pe \simeq 1950$, at which $-\mu_d(m = 1) \simeq 13.93$, while $-\mu_d(m = 2) \simeq 13.44$.

The values of μ_d depicted in figures 7 and 8 have been obtained by solving the corresponding generalized eigenvalue problem equation (3.3) for sufficiently large value of the number of modes, in order to ensure an accurate estimate of the dominant eigenvalue (details on the numerical solution of the generalized eigenvalue problem can be found in the Appendix A).

For all the operating conditions considered, the scaling $-\mu_d$ with Pe exhibits a complex structure characterized by the occurrence of intermediate power law scalings, and, asymptotically, (i.e. for $Pe \to \infty$) by a power law dependence

$$-\mu_d \sim \varepsilon_\alpha^\gamma \sim Pe^{-\gamma}, \qquad Pe \to \infty, \tag{4.1}$$

where the exponent γ $(0 < \gamma < 1)$ depends both on the geometry (ratio κ) and on the operating conditions (i.e. on Ω).

For example, for $\Omega = (0, 1)$, the large-gap geometry ($\kappa = 0.4$) yields an asymptotic exponent $\gamma = 1/2$, while the same operating conditions on a device with a larger inner radius ($\kappa = 0.8$) yields $\gamma = 1/4$.

Conversely, for $\Omega = (-1, 1)$, i.e. when the inner and outer cylinders are counter-rotating with the same absolute value of the angular velocity, the scaling $-\mu_d \sim Pe^{-1/3}$ characterizes the asymptotic behaviour of $-\mu_d$ independently of κ.

Table 1 summarizes the values of the asymptotic exponent γ for the cases depicted in figures 7 and 8. Apart from the asymptotic scaling, the behaviour of the dominant eigenvalue display a complex structure of intermediate power law scalings. Particularly interesting is the intermediate behaviour occurring for $\Omega = (-1, 1)$, which displays the scaling $-\mu_d \sim Pe^0$ that is persistent for almost two decades of the Péclet number. This is a significant result both from the practical and the theoretical point of view, since the behaviour $-\mu_d \sim$ constant is the best possible scenario for mixing that may arise from the interaction between advection and diffusion, not only in view of the high values of $-\mu_d$, which ensure swift axial homogenization of the stationary profile, but also because of the relative insensitivity of the device response to variations of the operating conditions (e.g. a change of flow rate or of the species diffusivity). In the case of closed flows, the independence of the homogenization exponents on Pe have been observed solely for globally chaotic flows (Giona *et al.* 2004*a*; Liu and Haller 2004*a*). Section 6 analyses in detail the occurrence of this behaviour. Another interesting observation is that the scaling of $-\mu_d$ versus Pe is not described by a

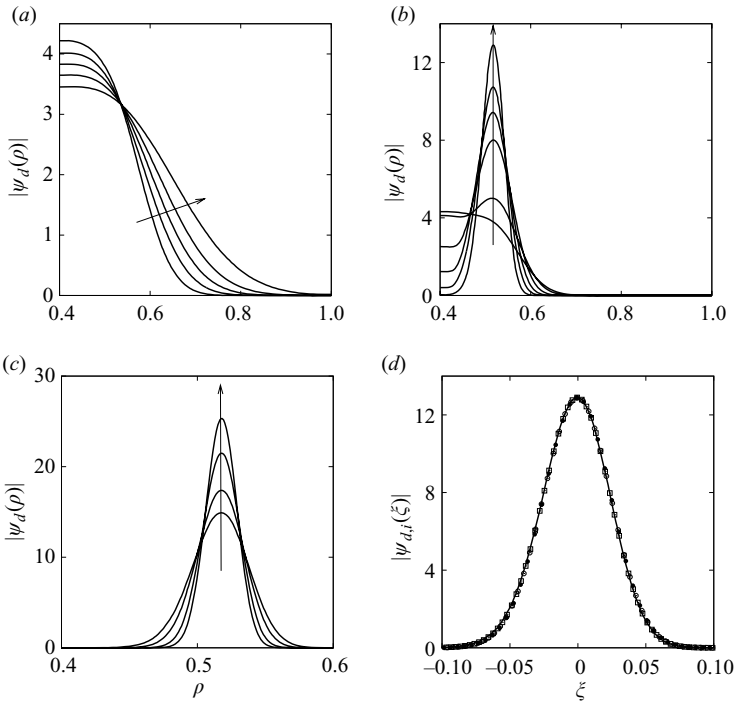

FIGURE 9. Modulus of the dominant convection-enhanced eigenfunction for $\kappa = 0.4$, $\Omega = (0, 1)$ ($\alpha = 6$, $\Gamma = \pi$). The arrows indicate increasing values of Pe. (*a*) $Pe = 2 \times 10^3,\ 5 \times 10^3,\ 10^4,\ 2 \times 10^4,\ 5 \times 10^4$. (*b*) $Pe = 10^5,\ 2 \times 10^5,\ 5 \times 10^5,\ 10^6,\ 2 \times 10^6,\ 5 \times 10^6$. (*c*) $Pe = 10^7,\ 2 \times 10^7,\ 5 \times 10^7,\ 10^8$. (observe that the abscissa range has changed with respect to *a*–*b*). (*d*) Invariant rescaling: $|\psi_{d,i}(\xi)|$ versus $\xi = (\rho - \rho^*)/\beta(\varepsilon_\alpha)$. The solid line refers to $Pe = 10^7$, while dots (□), (○), (●) to $Pe = 2 \times 10^7,\ 5 \times 10^7,\ 10^8$, respectively.

monotonically decreasing function of Pe. This seemingly counter intuitive result has been also observed in closed micromixers possessing cylindrical symmetry (Gleeson *et al.* 2004).

The best mixing performance is achieved for $\Omega = (-1, 1)$ in the range of $10^4 \leqslant Pe \leqslant 10^8$, giving rise to values of $-\mu_d$ of one or even two orders of magnitude greater than that associated with the protocol $\Omega = (0, 1)$.

4.2. *Eigenfunction localization*

The occurrence of several asymptotic regimes characterized by different numerical values of the exponent γ is a direct consequence of the different localization properties of the dominant eigenfunctions. This section describes the phenomenological aspects of localization, while the theoretical interpretation is discussed in §§ 5 and 6.

Consider first the case $\Omega = (0, 1)$, for which the potential $V(\rho)$ vanishes at the inner cylinder. Figure 9(*a*–*c*) depicts the modulus of the dominant eigenfunction $|\psi_d(\rho)|$ for different values of the Péclet number at $\kappa = 0.4$. For intermediate values of Pe, ranging from $Pe = 2 \times 10^3$ up to $Pe = 5 \times 10^4$ (figure 9*a*), the dominant eigenfunctions become progressively localized close to the inner cylinder. This Péclet range corresponds to the intermediate scaling (curve c) depicted in figure 7. For higher $Pe = (10^5, 5 \times 10^6)$ (figure 9*b*), a restructuring of the eigenfunction occurs. This Pe-range corresponds to the plateau in the scaling of $-\mu_d$ versus Pe connecting curve (c) to the asymptotic scaling (curve d) in figure 7. The eigenfunction moves progressively away from the

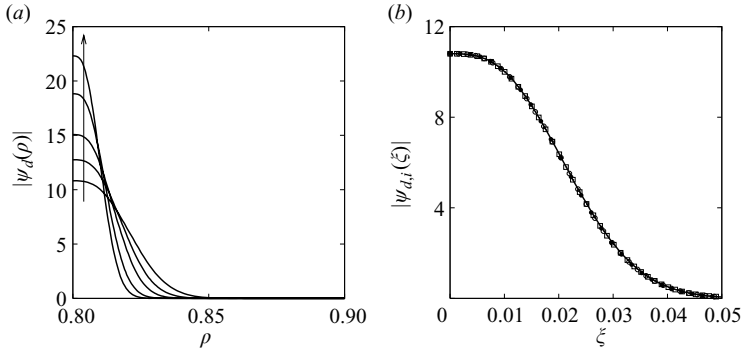

FIGURE 10. Modulus of the dominant convection-enhanced eigenfunction for $\kappa = 0.8$, $\Omega = (0, 1)$ ($\alpha = 6$, $\gamma = \pi$). The arrow indicates increasing values of Pe. (*a*) $Pe = 5 \times 10^6,\ 10^7,\ 2 \times 10^7, 5 \times 10^7,\ 10^8$. (*b*) Invariant rescaling: $|\psi_{d,i}(\xi)|$ versus $\xi = (\rho - \kappa)/\beta(\varepsilon_\alpha)$. The solid line refers to $Pe = 10^7$, while dots (□), (○), (●) to $Pe = 2 \times 10^7,\ 5 \times 10^7,\ 10^8$, respectively.

inner cylinder and becomes localized at an internal radial abscissa $\rho^* \simeq 0.518$ (a theoretical prediction of ρ^* is provided in §§ 5 and 6).

The asymptotic localization behaviour near ρ^* is depicted in figure 9(*c*). As in the case of the Couette plug flow the invariant rescaling in the asymptotic regime fulfils (3.11). The results are depicted in figure 9(*d*), and show an excellent agreement with (3.11).

The case $\Omega = (0, 1)$ for $\kappa = 0.8$ is depicted in figure 10. The real part of the dominant eigenfunction does not show intermediate scaling regimes. Starting from $Pe = 10^4$, the behaviour of $-\mu_d$ progressively sets onto an asymptotic behaviour expressed by (4.1) with $\gamma = 1/4$ (figure 8, curve c). The modulus of the dominant eigenfunction is depicted in figure 10(*a*), starting from $Pe = 5 \times 10^6$ (which is the value of Pe starting from which the asymptotic scaling of the eigenfunction is fully developed, see figure 8) up to $Pe = 10^8$. The eigenfunctions are localized at the wall of the inner cylinder, and satisfy the invariant rescaling (3.11). Eigenfunction invariance is depicted in figure 10(*b*).

The properties of the eigenfunctions change dramatically when the inner and the outer cylinder are counter-rotating, i.e. when $\Omega = (-1, 1)$. In this case, the potential $V(\rho)$ is different from zero at the walls of the flow device, while the axial velocity $w(\rho)$ vanishes on the inner and outer cylinder.

The modulus of the dominant eigenfunction is depicted in figure 11(*a*, *b*) for $\kappa = 0.4$, and figure 11(*d*, *e*) for $\kappa = 0.8$, respectively. Figures 11(*a*) and 11(*d*) refer to Péclet values corresponding to the spectral plateau depicted in figures 7, 8, corresponding to the scaling $-\mu_d \sim Pe^0$. Figures 11(*b*) and 11(*e*) refer to higher values of Pe giving rise to the asymptotic scaling $-\mu_d \sim Pe^{-1/3}$, shown in figure 7 and 8 (curve c).

The dominant eigenfunction becomes localized at an inner point ρ^* of the device, $\rho^* \simeq 0.672$ for $\kappa = 0.4$, and $\rho^* \simeq 0.899$ for $\kappa = 0.8$ (theoretical prediction of the localization radius is discussed in § 6). However, the transition towards the asymptotic localization displays a different phenomenology with respect to the case $\kappa = 0.4$, $\Omega = (0, 1)$, depicted in figure 9.

The intermediate transient regime occurring for $\Omega = (-1, 1)$, and characterized by the scaling $-\mu_d \sim$ constant, (curves a in figures 7 and 8), already displays eigenfunction localization towards an internal point close to ρ^*. The transition from intermediate

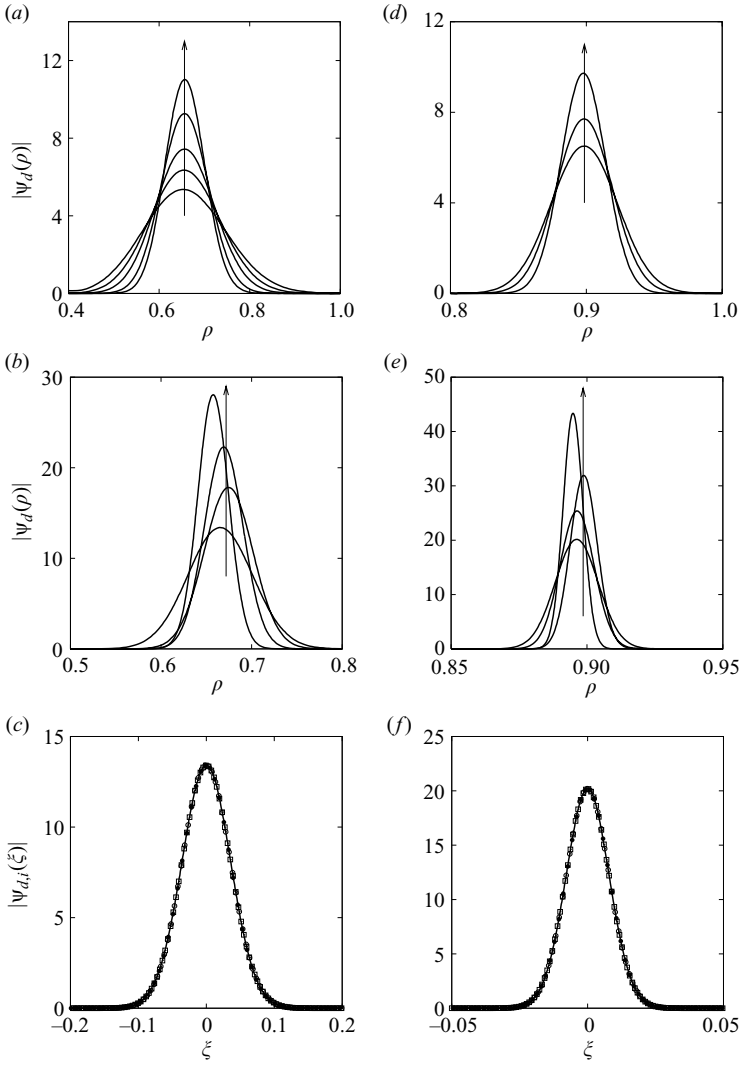

FIGURE 11. Modulus of the dominant convection-enhanced eigenfunction for $\Omega = (-1, 1)$ ($\alpha = 6$, $\Gamma = \pi$). (*a*)–(*c*) $\kappa = 0.4$, (*d*)–(*f*) $\kappa = 0.8$. (*a*), (*b*), (*d*), (*e*) The arrows indicate increasing values of Pe. (*a*) $Pe = 5\times10^3,\ 10^4,\ 2\times10^4,\ 5\times10^4,\ 10^5$. (*b*) $Pe = 2\times10^5,\ 5\times10^5,\ 10^6, 2\times10^6$. (*c*) Invariant rescaling $|\psi_{d,i}(\xi)|$ versus $\xi = (\rho - \rho_m(\varepsilon_\alpha))/\beta(\varepsilon_\alpha)$. The solid line refers to $Pe = 5 \times 10^5$, while dots (□), (○), (●) to $Pe = 10^6,\ 2 \times 10^6,\ 5 \times 10^6$, respectively. (*d*) $Pe = 10^5,\ 2 \times 10^5,\ 5 \times 10^5$. (*e*) $Pe = 5 \times 10^6,\ 10^7,\ 2 \times 10^7, 5 \times 10^7$. (*f*) Invariant rescaling: $|\psi_{d,i}(\xi)|$ versus $\xi = (\rho - \rho_m(\varepsilon_\alpha))/\beta(\varepsilon_\alpha)$. The solid line refers to $Pe = 10^7$, while dots (□), (○), (●) to $Pe = 2 \times 10^7,\ 5 \times 10^7,\ 10^8$, respectively.

to asymptotic regimes, corresponding to curve (a) and (b) in figure 8, is a peculiar phenomenon suggesting the presence of a dynamic instability, the details of which are described in § 6.

The graph of the eigenfunction modulus depicted in figures 11 (*b*) and 11(*e*) shows that the values of ρ^* at which the eigenfunction becomes localized in the Pe-asymptotic regime display a weak dependence on Pe, and it is convenient to use the notation $\rho^*(\varepsilon_\alpha)$ to indicate explicitly this dependence. The value of $\rho^*(\varepsilon_\alpha)$ oscillates in

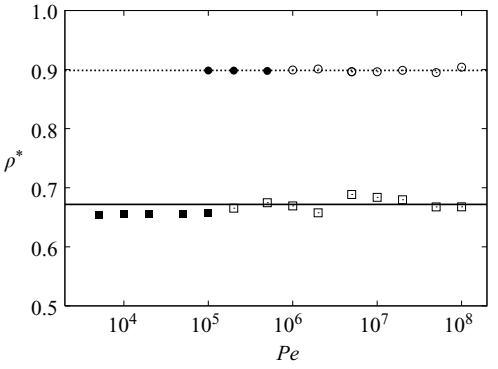

FIGURE 12. ρ^* versus Pe for $\Omega = (-1, 1)$. Dots are numerical results (■, □) for $\kappa = 0.4$, (●, ○) for $\kappa = 0.8$. Horizontal lines (solid for $\kappa = 0.4$, dashed for $\kappa = 0.8$) are the theoretical predictions (see § 6). Filled symbols (■, ●) correspond to the intermediate mixing regime, open symbols (□, ○) to the asymptotic scaling.

a complex way around a well defined mean value ($\rho^* = 0.672$ for $\kappa = 0.4$, $\rho^* = 0.899$ for $\kappa = 0.8$). This phenomenon is depicted in figure 12. In point of fact, these small fluctuations of the localization abscissa are not due to numerical inaccuracy, but rather on a peculiar phenomenon controlling the selection of the dominant eigenvalue. This issue is further addressed in § 6. As in all the cases previously considered, the invariant rescaling (3.11) applies also in this case, as depicted in figures 11(b) and 11(f). We emphasize that in the rescaling of the dominant eigenfunctions onto a single invariant master curve we have used for ρ^*, the value $\rho^*(\varepsilon_\alpha)$ of the radial abscissa of the mode of the modulus of the corresponding eigenfunction.

The information deriving from the analysis of the eigenfunction moduli should be complemented with the analysis of the behaviour of their real and imaginary part. Figure 13 depicts the real part of the eigenfunctions for all the cases considered in this section, at a characteristic value of Pe corresponding to the asymptotic scaling of the corresponding dominant eigenvalue. Since the eigenfunctions are generically complex-valued, their real part is obviously defined modulo a complex prefactor. The striking difference between the eigenfunctions for $\Omega = (0, 1)$ and for $\Omega = (-1, 1)$ is that while in the first case the structure of the real part has a major single peak with no oscillations, for $\Omega = (-1, 1)$ the real part of the eigenfunctions mimics a complex wavepacket. This phenomenological difference is associated with different properties of the phase of the eigenfunction which cannot be entirely understood by considering exclusively the eigenfunction moduli. A convenient strategy for tackling this problem is to apply a Bohmian decomposition of the eigenfunctions $\psi_d(\rho)$ into modulus and phase. This is developed in § 6.1.

5. Theoretical analysis

This section addresses the analysis of the spectral properties of the open Couette flow by focusing on the behaviour of the dominant convection-enhanced eigenvalue for large Pe (§§ 5.1 and 5.2). The starting point for predicting the asymptotic spectral scaling is the '*localization ansatz*' expressing the behaviour of the radial localization abscissa and its dependence on $V(\rho)$ and $w(\rho)$, which is justified in § 6.1.

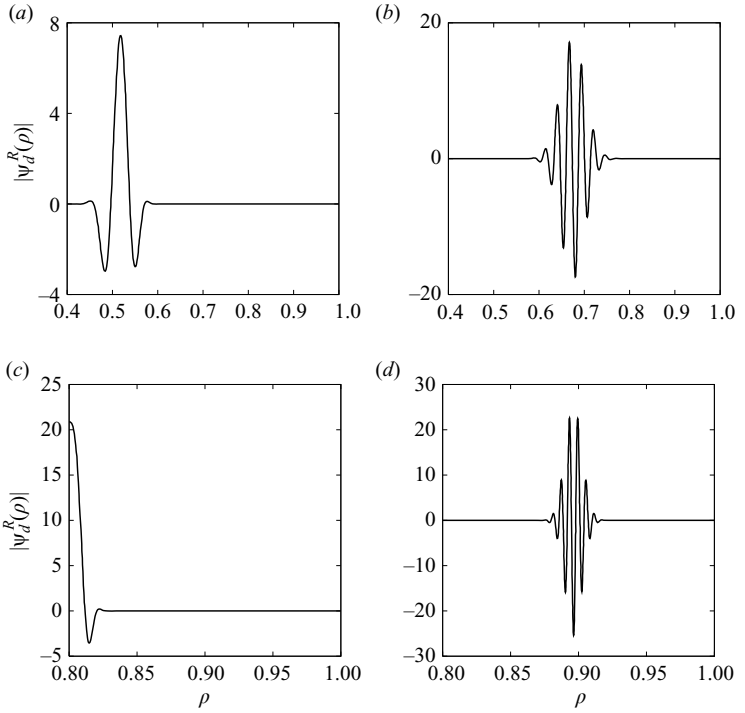

FIGURE 13. Real part of the dominant convection-enhanced eigenfunction. (*a*) $\kappa = 0.4$, $\Omega = (0, 1)$, $Pe = 10^7$. (*b*) $\kappa = 0.4$, $\Omega = (-1, 1)$, $Pe = 5 \times 10^5$. (*c*) $\kappa = 0.8$, $\Omega = (0, 1)$, $Pe = 10^8$. (*d*) $\kappa = 0.8$, $\Omega = (-1, 1)$, $Pe = 10^7$.

5.1. *Prediction of the asymptotic eigenvalue scaling*

The observed asymptotic scaling of the real part of the dominant convection-enhanced eigenvalue as a function of Pe described in § 4 can be interpreted by means of a simple *ansatz* on eigenfunction localization. To introduce this *ansatz*, it is convenient to reformulate (3.3) as

$$\lambda\,\psi(\rho) = \frac{\varepsilon_\alpha}{w(\rho)}\,\mathscr{D}_2[\psi](\rho) + i\,V_{eff}(\rho)\,\psi(\rho). \tag{5.1}$$

Equation (5.1) can be interpreted as a classical (non-generalized) eigenvalue problem in the presence of an effective potential

$$V_{eff}(\rho) = \frac{V(\rho)}{w(\rho)}, \tag{5.2}$$

which is the ratio of the angular to the axial velocity, and of a position dependent Péclet number $Pe_{eff}(\rho)$ given by $P_{eff}(\rho) = Pe\,w(\rho)$, which is the product of the Péclet number times the axial velocity. Since the axial velocity vanishes at the cylinder walls ($\rho = \kappa$, and $\rho = 1$), the effective Péclet number vanishes at the radial endpoints. Therefore the dimensionless effective diffusivity $1/Pe_{eff}(\rho)$ grows unbounded close to the inner and outer cylinders. The latter observation is physically evident, since the axial velocity vanishes at the inner and outer cylinders and, consequently, diffusion dominates near the solid boundaries.

From the discussion above, it is intuitive to expect that mixing properties of open Couette flow devices are controlled by the behaviour of the effective potential $V_{eff}(\rho)$ and of the effective Péclet number $P_{eff}(\rho)$.

The *localization ansatz*, that should be so far considered as a conjecture on the behaviour the dominant convection-enhanced eigenfunctions, can be stated by considering the properties of the effective potential $V_{eff}(\rho)$. Suppose that $V_{eff}(\rho)$ admits a local bounded extremal value at ρ_1 (local maximum or minimum) or a bounded absolute extremal value at the boundary $\rho = \rho_2$. Let $V_{eff}(\rho) - V_{eff}(\rho_h) \sim (\rho - \rho_h)^{c_h}$, $h = 1, 2$ the local expansion of the effective potential close to the two extremal points ρ_h ($h = 1, 2$). The dominant convective eigenfunction becomes localized asymptotically at the radial abscissa $\rho = \rho^*$, where $\rho^* \in \{\rho_1, \rho_2\}$ corresponding to the highest value of local nonlinearity exponent c_h. If $c_1 = c_2$, localization occurs at the radial abscissa ρ_h ($h = 1, 2$) that yields the lowest value of $-\mu_d$.

Conversely, if the effective potential is a monotonic function of ρ, diverging to $\pm\infty$ at the interval boundaries, then the dominant convection-enhanced eigenfunction becomes localized at an internal radial abscissa ρ^* corresponding to the local extremal point of the function

$$\sigma(\rho) = w(\rho)\, V'_{eff}(\rho) = \frac{V'(\rho)\, w(\rho) - w'(\rho)\, V(\rho)}{w(\rho)}, \tag{5.3}$$

where $V'_{eff}(\rho) = \mathrm{d}V_{eff}(\rho)/\mathrm{d}\rho$. In point of fact, this result is strictly valid in the intermediate scaling region, where $-\mu_d \sim Pe^0$, while asymptotically, i.e. for very large Pe, it can be justified from kinematic arguments that the localization abscissa ρ^* corresponds to the minimum of $|V'_{eff}(\rho)|$. However, in the case of the Couette flow considered in this article, the minimum of $|V'_{eff}(\rho)|$ and the local extremal value of $\sigma(\rho)$ are so close to each other that they can be assumed practically coincident. This means that for this flow system the condition expressed by (5.3) can also be used to characterize the asymptotic scaling. A theoretical justification of the localization based on $\sigma(\rho)$ is developed in § 6.

The first part of this ansatz corresponds to what already observed and discussed for closed flow systems (Giona *et al.* 2004*b*,*c*). A theoretical justification of the second part of the localization ansatz is developed in § 6.1.

Before applying this conjecture for deriving the scaling properties of the dominant convective eigenvalue, let us illustrate it for the specific class of flow protocols considered throughout the article. Figure 14 depicts the behaviour of $V_{eff}(\rho)$ and $\sigma(\rho)$ in these cases.

For $\kappa = 0.4$ and $\Omega = (0, 1)$ (figures 14*a* and 14*b*), $V_{eff}(\rho)$ is bounded close to $\rho = \kappa$, since both $V(\rho)$ and $w(\rho)$ vanish at that point. The effective potential also admits a local quadratic minimum at an internal point, $\rho^* = 0.518$. The localization conjecture predicts that the dominant convection-enhanced eigenfunction should become localized asymptotically at ρ^*, and this is exactly what has been observed in the numerical simulations (figure 9). Consider the case $\kappa = 0.8$, $\Omega = (0, 1)$ (figure 14*e*–*f*). The function $V_{eff}(\rho)$ is monotonically increasing with ρ and possesses a bounded extremal value at $\rho = \kappa$. Consequently, the localization ansatz predicts that the dominant convection-enhanced eigenfunctions become localized at the inner cylinder radius, as observed in figure 10.

Let us now focus on the rotation condition $\Omega = (-1, 1)$, which admits no analogous for closed flows. For any $\kappa > 0$, (and specifically for $\kappa = 0.4$ and $\kappa = 0.8$ depicted in figure 14*c* and 14*g*, respectively), $V_{eff}(\rho)$ is a monotonically increasing function of ρ,

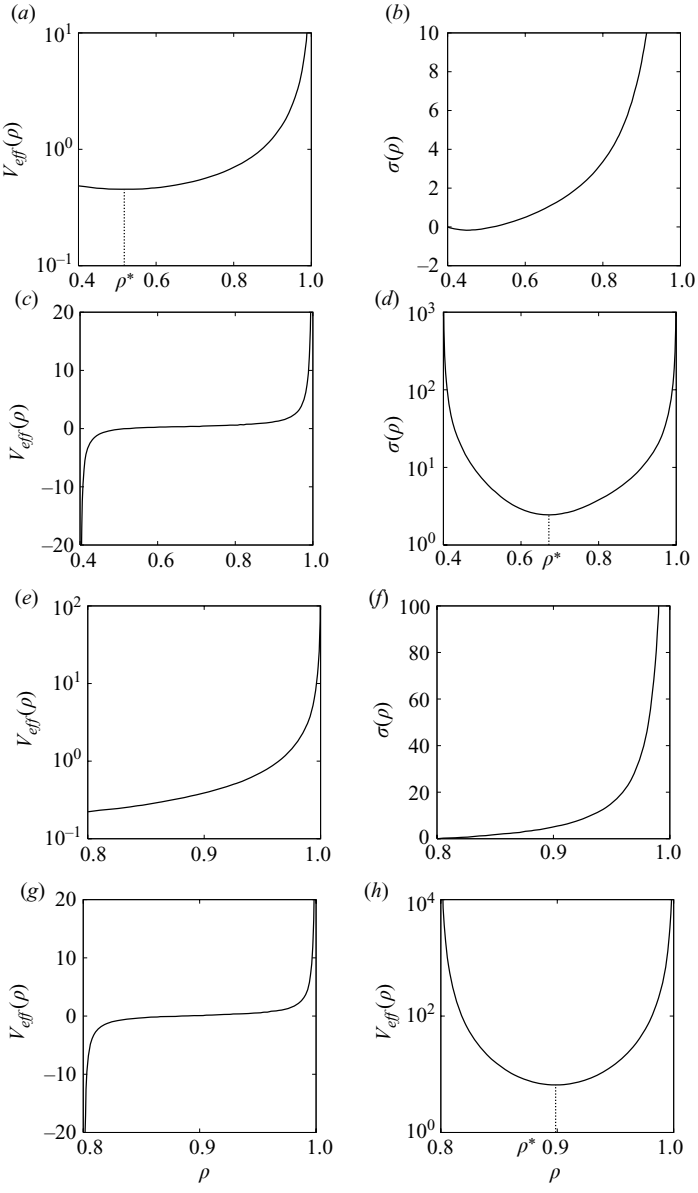

FIGURE 14. $V_{eff}(\rho)$ and $\sigma(\rho)$ for different flow configurations. (*a*)–(*b*) $\kappa = 0.4$, $\Omega = (0, 1)$. (*c*)–(*d*) $\kappa = 0.4$, $\Omega = (-1, 1)$. (*e*)–(*f*) $\kappa = 0.8$, $\Omega = (0, 1)$. (*g*)–(*h*) $\kappa = 0.8$, $\Omega = (-1, 1)$.

diverging to $-\infty$ for $\rho \to \kappa$, and to ∞ for $\rho \to 1$. The localization ansatz in these cases states that the localization abscissa ρ^* corresponds to the local extremal value of $\sigma(\rho)$ (a local minimum of $w(\rho)\, V'_{eff}(\rho)$ as depicted in figure 14*d* and 14*h*). The local minimum of $\sigma(\rho)$ occurs for $\rho^* = 0.672$ for $\kappa = 0.4$, and $\rho^* = 0.899$ for $\kappa = 0.8$, in agreement with the numerical simulations (see figure 12).

Although stated in the form of a conjecture, the localization ansatz explains satisfactorily the occurrence of difference localization points in the open Couette flow. While the first part of this conjecture (i.e. when $V_{eff}(\rho)$ admits a bounded extremal value) is equivalent to the analysis developed for closed flows (see e.g. Giona

κ	Ω	ρ^*	δ	ν	γ
0.4	(0, 1)	Inner point	2	0	1/2
0.4	(−1, 1)	Inner point	1	0	1/3
0.8	(0, 1)	κ	1	1	1/4
0.8	(−1, 1)	Inner point	1	0	1/3

TABLE 2. Localization point ρ^*, flow exponents δ and ν, and theoretical prediction for γ based on (5.5) for the different geometric and operating conditions considered throughout this article.

et al. 2004*b*,*c*), the less intuitive part of the conjecture, which is specific of open flow systems and finds no counterpart in closed flows, is justified in § 6.1.

The details of the calculations for predicting the scaling exponent γ in each flow condition occurring for the open Couette flow is reported in Appendix B. By using the same technique applied in Appendix B, it is possible to obtain a general scaling result. Let ρ^* be the localization abscissa in the neighbourhood of which $w(\rho)$ and $V_{eff}(\rho)$ behave to the leading order as

$$w(\rho) = w_0\,(\rho-\rho^*)^{\nu}+O(|\rho-\rho^*|^{\nu+1}), \quad V_{eff}(\rho) = a_0+a_1\,(\rho-\rho^*)^{\delta}+O(|\rho-\rho^*|^{\delta+1}). \tag{5.4}$$

The scaling exponent γ entering (4.1) is a function of the exponents ν and δ defined by (5.4) and reads

$$\gamma = \frac{\delta}{2+\nu+\delta}. \tag{5.5}$$

Table 2 reviews the values of the exponents δ, ν and the prediction for γ deriving from (5.5) that are in agreement with the numerical observations.

5.2. *Spectral phase transitions and mixing regimes*

The analysis developed in the previous paragraph for $\Omega = (0, 1)$ indicates that the geometry, and specifically the parameter κ, induces a qualitative change in the spectral behaviour of the advection–diffusion equation associated with the open Couette flow. Henceforth we use the wording '*spectral phase transition*' to indicate a sharp change in the asymptotic spectral scaling of the dominant eigenvalue at large Pe, which may occur when one or more geometric and operating parameters are varied.

The typical example of a spectral phase transition occurs for $\Omega = (0, 1)$, when the radius of the inner cylinder is increased. The phenomenology of this phase transition is qualitatively described by the graphs of $V_{eff}(\rho)$ depicted in figure 14(*a*, *e*). For sufficiently small values of κ below a critical threshold κ_c (which is estimated below), $V_{eff}(\rho)$ possesses a local extremal value at an internal radial abscissa $\rho^* > \kappa$. In this condition, the dominant convection-enhanced eigenvalue scales as $-\mu_d \sim Pe^{-1/2}$. When κ is increased, (e.g. for $\kappa = 0.8$) the graph of $V_{eff}(\rho)$ becomes monotonic with ρ, and the dominant convection-enhanced eigenfunction becomes localized at $\rho = \kappa$, giving rise to the scaling $-\mu_d \sim Pe^{-1/4}$. This suggests that the characteristic function of this spectral phase transition is the first derivative of $V_{eff}(\rho)$ at $\rho = \kappa$,

$$G(\kappa) = \lim_{\rho\to\kappa} \frac{\mathrm{d}V_{eff}(\rho)}{\mathrm{d}\rho}. \tag{5.6}$$

The critical inner cylinder radius κ_c is therefore given by the value of κ at which $G(\kappa)|_{\kappa=\kappa_c} = 0$. The function $G(\kappa)$ attains negative values for $\kappa < \kappa_c$, and positive values for $\kappa = \kappa_c$. Figure 15(*a*) depicts the behaviour of $G(\kappa)$ versus κ. Simple algebraic

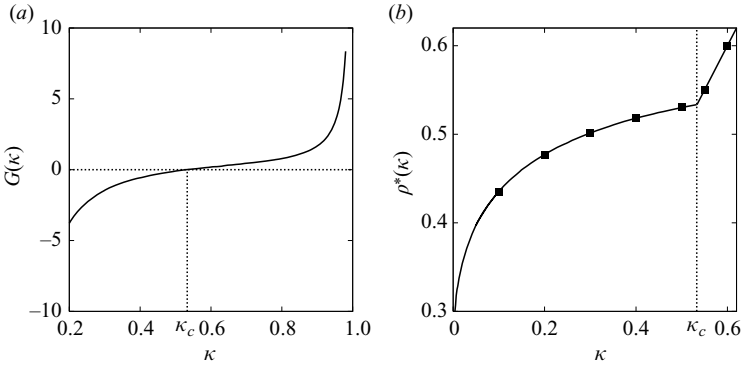

FIGURE 15. Representation of the spectral phase transition occurring for the open Couette flow at $\Omega = (0, 1)$. ($\alpha = 6$, $\Gamma = \pi$). The parameter κ_c represents the critical radius. (a): $G(\kappa)$ versus κ. (b): $\rho^*(\kappa)$ versus κ. Dots (●) represent the radial localization abscissa obtained from the numerically computed eigenfunctions. The solid line is the prediction of the localization ansatz.

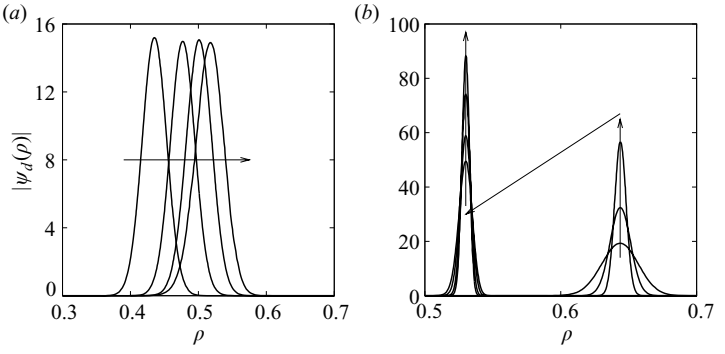

FIGURE 16. Localization of the dominant eigenfunction for values of $\kappa < \kappa_c$ for $\Omega = (0, 1)$. (a) Dominant convective eigenfunction at $Pe = 10^7$ for increasing values of $\kappa = 0.1$, 0.2, 0.3, 0.4 (in the direction of the arrow). (b) $\kappa = 0.5$. The arrows indicate increasing values of Pe: $Pe = 10^7$, 10^8, 10^9 (localized around $\rho = 0.643$), and $Pe = 10^{10}$, 2×10^{10}, 5×10^{10}, 10^{11} (localized around the asymptotic value $\rho^* = 0.530$).

manipulations show that the equation $G(\kappa) = 0$ simplifies to

$$1 - \kappa^2 + 4\kappa^2 \log \kappa = 0 \tag{5.7}$$

from which the value $\kappa_c = 0.533$ can be obtained. Let us analyse the localization behaviour close to the transition point κ_c. Figure 15(b) depicts the value of the localization abscissa $\rho^*(\kappa)$ as a function of κ, and compares the theoretical prediction for $\rho^*(\kappa)$ deriving from the localization ansatz with the numerical results of eigenfunction localization. The function $\rho^*(\kappa)$ can be viewed as the order parameter of this spectral phase transition. At the transition point κ_c, $\rho^*(\kappa)$ is continuous but not differentiable.

The localization properties of the eigenfunctions for $\kappa < \kappa_c$ far from the critical point are depicted in figure 16(a). More interesting is the spectral behaviour close to the transition point κ_c. Figure 17 shows the behaviour of the dominant convection-enhanced eigenvalues μ_d as a function of Pe for κ slightly below ($\kappa = 0.5$) and above ($\kappa = 0.6$) the transition point. As expected, the dominant eigenvalue scales

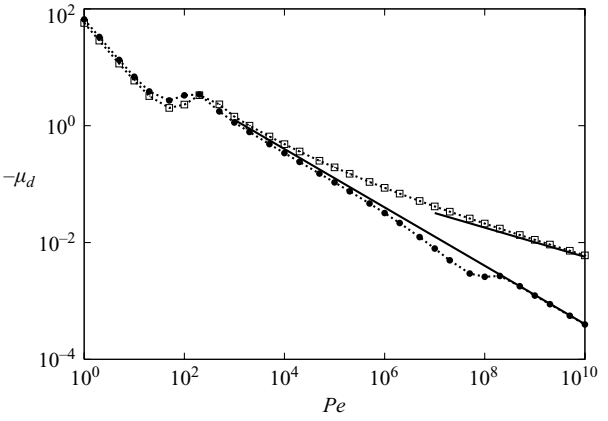

FIGURE 17. Real part of the dominant convection-enhanced eigenvalue μ_d versus Pe for the Couette flow at $\Omega = (0, 1)$. Dots (●) refer to $\kappa = 0.5$ (below the spectral phase transition), (□) to $\kappa = 0.6$ (above the transition). Upper and lower solid lines correspond to the scalings $-\mu_d \sim Pe^{-1/4}$ and $-\mu_d \sim Pe^{-1/2}$, respectively.

asymptotically in a different way above and below κ_c. The relaxation towards the asymptotic scaling is peculiar for $\kappa = 0.5$, and requires further analysis. The Péclet range $Pe = (10^2, 10^6)$ is still characterized by transient spectral phenomena. In the range $Pe = (10^6, 10^9)$, the spectrum undergoes a restructuring, and solely starting from $Pe > 10^9$, the asymptotic scaling is attained. At present, a theory predicting the critical Péclet value corresponding to the onset of the asymptotic localization regime is not available.

The phenomenology of this complex relaxation towards the asymptotic regime can be explained by considering the localization properties of the dominant eigenfunctions, depicted in figure 16(*b*). For $Pe < 10^9$, the dominant eigenfunction shows a transient localization at an internal point $\rho = 0.643$. It is necessary to consider higher values of $Pe > 10^{10}$ to observe the asymptotic localization around $\rho^* = 0.530$, corresponding to the local extremal value of $V_{eff}(\rho)$.

This example shows that there are cases where the asymptotic scaling can manifest itself at very large values of the Peclect number (e.g. $Pe \sim 10^9$), and therefore a careful attitude must be adopted when analysing the asymptotic spectral properties.

Different types of spectral phase transitions can occur by changing the operating conditions. For example, one can consider the inner cylinder angular velocity as a parameter, and study the flow configurations $\Omega = (\omega, 1)$ where $\omega \in (-\omega_1, \omega_1)$, $\omega_1 > 0$. This corresponds to study the qualitative behaviour of the system when the direction of the relative motion of the two cylinders is inverted.

For negative values of ω, the situation is similar to the case $\Omega = (-1, 1)$, and gives rise to localized eigenfunction at an inner point ρ^* corresponding to the local extremal point of $\sigma(\rho)$ (according to the localization ansatz). In these conditions, the scaling exponent is $\gamma = 1/3$.

The value $\omega_c = 0$ is the critical point. Depending on the value of κ, above ω_c the dominant convective eigenfunctions becomes asymptotically localized either at the inner cylinder radius, or at an internal point ρ^*, corresponding to the local extremal point of $V_{eff}(\rho)$. This phenomenon depends on the phase transition discussed above. Consequently, the exponent γ attains for $\omega = 0$ either the value 1/4 or 1/2. For

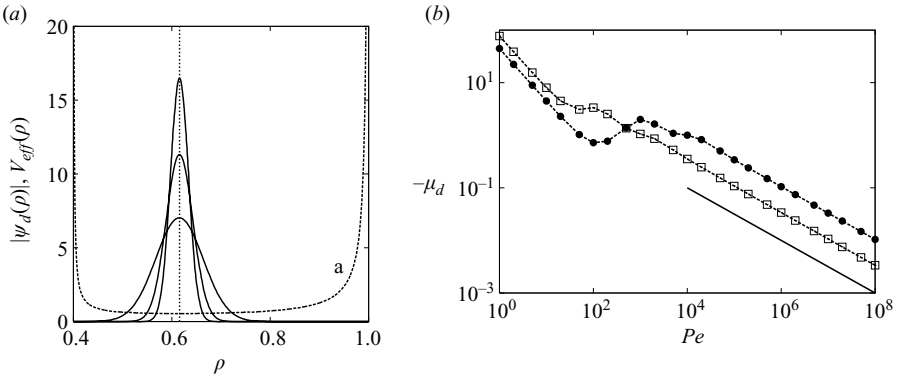

FIGURE 18. (*a*) $|\psi_d(\rho)|$ versus ρ for $\kappa = 0.4$, $\Omega = (0.3, 1)$, for three different values of $Pe = 10^5,\ 10^6,\ 5 \times 10^6$. The dashed line (a) is the graph of the effective potential $V_{eff}(\rho)$. The dotted vertical line is centred at the local minimum of $V_{eff}(\rho)$. (*b*) Real part of the dominant convection-enhanced eigenvalue μ_d versus Pe for $\Omega = (0.3, 1)$ for $\kappa = 0.4$ (□), and for $\kappa = 0.8$ (●). The solid line corresponds to the scaling $-\mu_d \sim Pe^{-1/2}$ predicted by the localization theory.

positive ω, both the inner and the outer cylinders are set in motion. The resulting effective potential becomes singular for $\rho = \kappa$, and $\rho = 1$, diverging to ∞.

Therefore, the graph of $V_{eff}(\rho)$ displays a local minimum at an inner point ρ^*, as depicted in figure 18(*a*). The dominant convection-enhanced eigenfunction becomes asymptotically localized at $\rho = \rho^*$ and, from what discussed in § 5.1 (this case is analogous to the condition $\kappa = 0.4$, $\Omega = (0, 1)$), the scaling exponent γ should attain the value $\gamma = 1/2$. Figure 18(*b*) shows the scaling of μ_d versus Pe for $\omega = 0.3$, and for two different values of $\kappa = 0.4,\ 0.8$. Numerical results are in agreement with the localization theory, and this is a further confirmation of the localization ansatz.

6. Fine spectral structure for the protocol $\Omega = (-1, 1)$

In this section, a detailed analysis of the spectral properties associated with flow protocols characterized by a counter-rotating cylinder motion is developed. Specifically, the case $\Omega = (-1, 1)$ is considered.

6.1. *Bohmian decomposition and localization*

The localization ansatz predicts different localization properties depending on whether the effective potential $V_{eff}(\rho)$ possesses bounded extrema or not. In the first case, the localization behaviour of the dominant convection-enhanced eigenfunction is analogous to that associated with closed bounded autonomous flows. Besides, in the case of a monotonic potential $V_{eff}(\rho)$, diverging at the boundary points, the analysis involves the function $\sigma(\rho)$ defined by (5.3), the physical meaning of which is far from being intuitive.

To explain this part of the localization conjecture, consider (3.3). For large Pe, the diagonal term $-\varepsilon_\alpha m^2 \psi(\rho)/\rho^2$ can be neglected so that (3.3) simplifies to

$$\lambda\, w(\rho)\, \psi(\rho) = \frac{\varepsilon_\alpha}{\rho} \frac{\mathrm{d}}{\mathrm{d}\rho} \left(\rho\, \frac{\mathrm{d}\psi(\rho)}{\mathrm{d}\rho} \right) + i\, V(\rho)\, \psi(\rho). \tag{6.1}$$

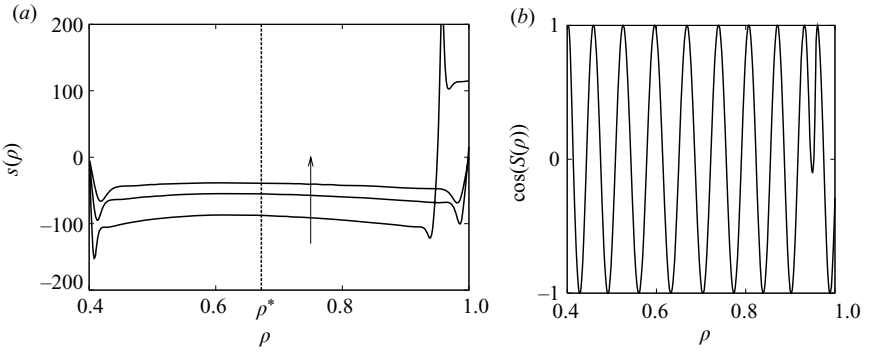

FIGURE 19. Behaviour of the phase derivative $s(\rho)$ versus ρ for $\kappa = 0.4$, $\Omega = (-1, 1)$ for several values of $Pe = 10^4,\ 2 \times 10^4,\ 5 \times 50^4$ (Pe increases in the direction of the arrow). (B) $\cos(S(\rho))$ versus ρ for $Pe = 5 \times 10^4$.

Let us introduce the factorization of the eigenfunction in terms of modulus $h(\rho)$ and phase $S(\rho)$,

$$\psi(\rho) = h(\rho) \mathrm{e}^{i\, S(\rho)}. \tag{6.2}$$

The decomposition equation (6.2) is identical to that used by Bohm for deriving his formulation of quantum mechanics (Bohm 1952), and for this reason it will be referred to as the *Bohmian decomposition.*

Substituting (6.2) into (6.1), and letting $\lambda = \mu + iq$, a system of two differential equations for $h(\rho)$ and $S(\rho)$ is obtained

$$\mu\, w(\rho)\, h(\rho) = \frac{\varepsilon_\alpha}{\rho} \left[(\rho\, h'(\rho))' - \rho\, h(\rho)(S'(\rho))^2\right], \tag{6.3}$$

$$q\, w(\rho)\, h(\rho) = \frac{\varepsilon_\alpha}{\rho} \left[h(\rho)\, S'(\rho) + 2\,\rho\, h'(\rho)\, v S'(\rho) + \rho\, h(\rho)\, S''(\rho)\right] + V(\rho)\, h(\rho). \tag{6.4}$$

The terms entering (6.4) can be rearranged in the form

$$h'(\rho) = \left[\frac{q\, w(\rho) - V(\rho)}{2\varepsilon_\alpha\, S'(\rho)} - \frac{S''(\rho)}{2S'(\rho)} - \frac{1}{2\rho}\right] h(\rho), \tag{6.5}$$

which can be integrated to give the formal solution

$$h(\rho) = \frac{h_0}{\sqrt{\rho\, |S'(\rho)|}} \exp\left[\int^{\rho} \frac{q\, w(\xi) - V(\xi)}{2\varepsilon_\alpha\, S'(\xi)}\, \mathrm{d}\xi\right], \tag{6.6}$$

where h_0 is a constant. Let us introduce a simplifying assumption, namely the *constant phase variation approximation.* This means that, close to the localization point, the phase derivative $s(\rho) = S'(\rho)$ is a slow varying function of ρ that can be approximated by a constant $s_0 \neq 0$,

$$s(\rho) = S'(\rho) = s_0 = \text{constant}. \tag{6.7}$$

Equation (6.7) is consistent with the numerical results at $\Omega = (-1, 1)$. Figure 19(a) depicts the graph of the phase derivative $s(\rho)$ versus ρ of the dominant convection-enhanced eigenfunctions for $\kappa = 0.4$.

As can be observed, close to $\rho = \rho^*$ (marked by a dashed vertical line), $s(\rho) = S'(\rho)$ is constant, and remains practically constant in the interval, centred at ρ^*, in which $h(\rho)$ is significantly different from zero ($h(\rho) > 10^{-8}\, h(\rho^*)$). This gives rise to a phase

contribution $e^{i\,S(\rho)} \simeq e^{i\,s_0\rho}$ which is an almost perfect sinusoidal function in the region where $h(\rho)$ is different from zero (figure 19*b*).

With the aid of (6.7), (6.6) simplifies to

$$h(\rho) = \frac{h_0}{\sqrt{\rho\,|s_0|}}\,\exp\left\{\frac{1}{2s_0\varepsilon_\alpha}\left[q\int_{\rho^*}^{\rho} w(\xi)\mathrm{d}\xi - \int_{\rho^*}^{\rho} V(\xi)\mathrm{d}\xi\right]\right\} = \frac{h_0}{\sqrt{\rho\,|s_0|}}\exp\left[\frac{1}{2s_0\varepsilon_\alpha}\Phi(\rho,\rho^*)\right] \tag{6.8}$$

Neglecting the $\rho^{-1/2}$ dependence with respect to the exponential, the extremal point of $h(\rho)$ corresponds to $\Phi(\rho,\rho^*)|_{\rho=\rho^*}=0$. This condition can be made explicit to give $q\,w(\rho^*)-V(\rho^*)=0$, which implies that the imaginary part of the eigenvalue q is given by

$$q = \frac{V(\rho^*)}{w(\rho^*)}. \tag{6.9}$$

Equation (6.9) is consistent with (3.9) for a localized eigenfunction at $\rho=\rho^*$. It follows from (6.9) that $\Phi(\rho,\rho^*)$ can be expressed as

$$\Phi(\rho,\rho^*) = \frac{V(\rho^*)}{w(\rho^*)}\int_{\rho^*}^{\rho} w(\xi)\,\mathrm{d}\xi - \int_{\rho^*}^{\rho} V(\xi)\,\mathrm{d}\xi. \tag{6.10}$$

Let us expand $\Phi(\rho,\rho^*)$ in Taylor series of ρ at ρ^*. Since $\Phi(\rho^*,\rho^*)=0$, $\Phi'(\rho,\rho^*)|_{\rho=\rho^*}=0$, one obtains

$$\Phi(\rho,\rho^*) = -\frac{1}{2}\sigma(\rho^*)(\rho-\rho^*)^2 - \frac{1}{6}\sigma'(\rho^*)(\rho-\rho^*)^3 + O(|\rho-\rho^*|^4), \tag{6.11}$$

where the function $\sigma(\rho)$ is defined by (5.3). In order to ensure that that $h(\rho)<h(\rho^*)$, the function $\Phi(\rho,\rho^*)$ should be locally quadratic and even when expressed in terms of $\rho-\rho^*$ in an interval centred at ρ^*. This implies

$$\sigma'(\rho)|_{\rho=\rho^*} = 0, \tag{6.12}$$

which is the claim of the localization ansatz stated in § 5.1. It is possible to provide another derivation of (6.12). From (6.5), neglecting the term $1/2\rho$, assuming the constant phase-variation approximation, and expanding $w(\rho)$ and $V(\rho)$ in power series, it follows that

$$h'(\rho)/h(\rho) \simeq -(1/2\varepsilon_\alpha s_0)[V'(\rho^*)-V(\rho^*)\,w'(\rho^*)/w(\rho^*)](\rho-\rho^*)+O(|\rho-\rho^*|^2). \tag{6.13}$$

The localization abscissa that provides the greatest dominant eigenvalue corresponds to the value of ρ^* for which the term between square parentheses is minimum, which corresponds to condition (6.12).

The validity of (6.11), (6.12) is further confirmed by observing that the profile of the dominant convection-enhanced eigenfunction is strictly Gaussian for $\Omega=(-1,1)$, as depicted in figure 20.

The analysis developed above provides a justification of the second statement of the localization ansatz when $V_{eff}(\rho)$ is monotonic and unbounded at the walls. It is useful to point out that the validity of (6.12) is based on the assumption of constant phase variation, close to the localization point. While this assumption applies for $\Omega=(-1,1)$ (as demonstrated by the numerical simulations), i.e. when $V_{eff}(\rho)$ is a monotonic function of its argument, the constant phase variation approximation fails for $\Omega=(0,1)$, and this is the reason why (6.12) cannot be taken as the mathematical formulation of the localization ansatz in these cases.

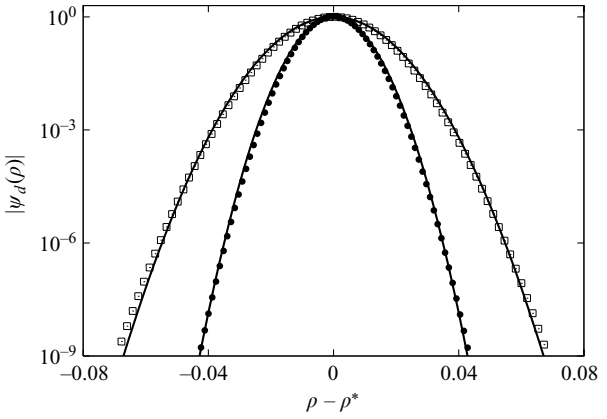

FIGURE 20. Log-normal plot of the modulus of $|\psi_d(\rho)|$ versus $\rho - \rho^*$ for $\Omega = (-1, 1)$ at $Pe = 10^7$. The eigenfunction is normalized so that its maximum equals 1. Dots (□) refers to $\kappa = 0.4$, (●) to $\kappa = 0.8$. The solid lines are the Gaussian approximations $\exp(-b\,\rho^2)$, where b is a parameter that depends on κ and Pe.

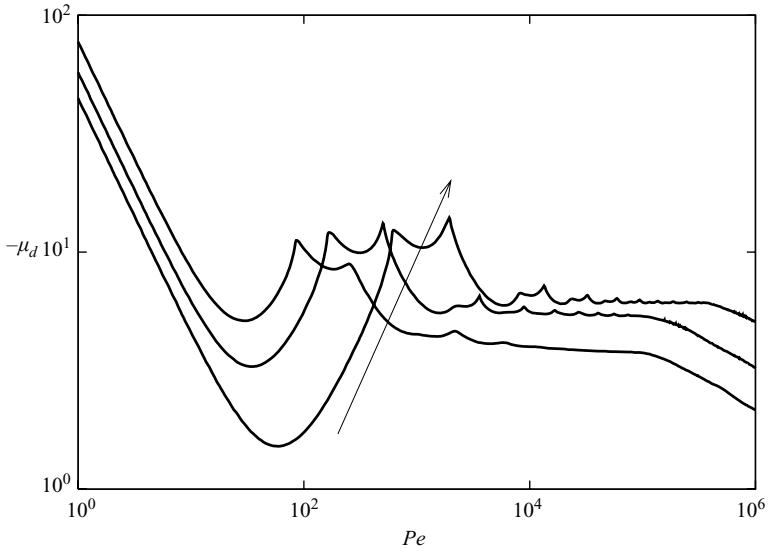

FIGURE 21. Real part of the dominant eigenvalue as a function of the Péclet number for $\alpha = 6$, $\Gamma = \pi$, $\Omega = (-1, 1)$. The arrow indicates increasing values of $\kappa = 0.4,\ 0.6,\ 0.8$.

6.2. *Global spectral structure and selection rules*

One of the most peculiar features of the Couette flow at $\Omega = (-1, 1)$ is the occurrence, for intermediate Péclet values (spanning more than two decades), of a plateau in the graph of $-\mu_d$ versus Pe, at which the real part of dominant convection-enhanced eigenvalue attains substantially a constant value, as depicted in figure 21 for several values of κ. The condition $-\mu_d \sim Pe^0$ is optimal for mixing, and has been observed for closed flows giving rise to globally chaotic kinematics (Toussaint *et al.* 1995; Cerbelli *et al.* 2004; Liu and Haller 2004*a*,*b*). In this section, we investigate further the spectral properties in this intermediate region of Péclet numbers.

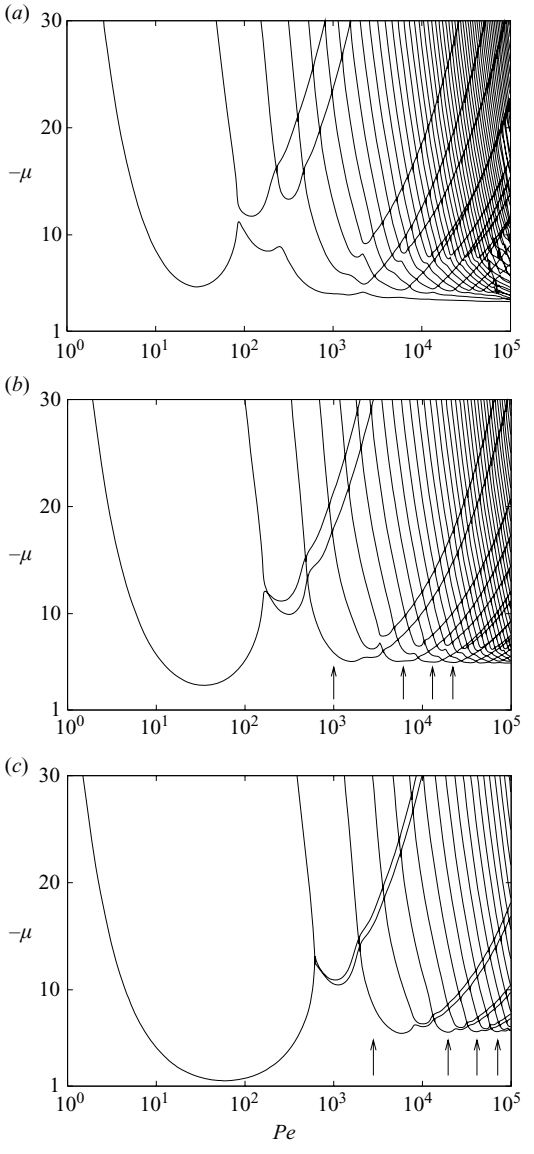

FIGURE 22. Real part of the eigenvalue spectrum as a function of the Péclet number for $\alpha = 6$, $\Gamma = \pi$, $\Omega = (-1, 1)$. (*a*) $\kappa = 0.4$, (*b*) $\kappa = 0.6$, (*c*) $\kappa = 0.8$.

Let us consider in more detail the behaviour of $-\mu_d$ depicted in figure 21 in the Péclet range $(5\times10^3, 5\times10^5)$. Even though $-\mu_d$ is practically constant, complex, small-amplitude oscillations, and the occurrence of local cusps characterize the behaviour of $-\mu_d$ around the constant mean value. The origin of this complex behaviour (which is not due to numerics, but it is a property of the system) can be interpreted by considering the whole eigenvalue spectrum (for $m = 1$) the real part of which is depicted in figure 22(*a–c*) for $\kappa = 0.4,\ 0.6,\ 0.8$, respectively.

The eigenvalue spectrum, parametrized with respect to Pe, can be considered as the union of a countable family of branches $\{b_h(Pe)\}$. A natural ordering amongst the spectral branches can be defined by considering the behaviour at low Péclet values

($Pe < 1$), i.e. in the diffusive regime. Indeed, for $Pe < 1$,

$$b_h(Pe) \simeq \mu_h^{(0)} \varepsilon_\alpha , \qquad h = 1, 2, \ldots , \tag{6.14}$$

where $\mu_1^{(0)} > \mu_2^{(0)} > \cdots \mu_n^{(0)} > \cdots$, and $\mu_h^{(0)} < 0$, $h = 1, 2, \ldots$ are the diffusive eigenvalues solution of the Hermitian eigenvalue problem $\mathscr{D}_2[\psi](\rho) = \mu^{(0)} w(\rho)\, \psi(\rho)$.

Each branch is the graph of a smooth function of Pe. At low Péclet values, the dominant convective eigenfunctions belong, by definition, to the first spectral branch $b_1(Pe)$. However, as Pe increases, the graphs of the real part of different spectral branches may intersect each other, giving rise to an exchange of dominance. These intersections give rise to the '*selection rule*' $[h \to k]$ with $h < k$. This means that there exists a value Pe^* such that for $Pe < Pe^*$, $\mu_d(Pe) = \Re[b_h(Pe)]$, while for $Pe > Pe^*$, $\mu_d(Pe) = \Re[b_k(Pe)]$. Here $\Re[b]$ indicates the real part of the complex number b. Therefore, at $Pe = Pe^*$ the real parts of the h and k branches cross each other, and consequently an exchange of dominance occurs between the two crossing branches.

The symbol $[h \to k]$ indicates the exchange of dominance occurring at some Pe^*. It is also clear the wording 'selection rule' to indicate this phenomenon: the dominant convection-enhanced eigenvalue is 'selected' by the actual Péclet value amongst the different spectral branches which are ordered according to their diffusive behaviour at low Pe.

Consider the spectral plot of the real part of the eigenvalues depicted in figure 22. For $\kappa = 0.4$, figure 22(a), no exchange of dominance between spectral branches is observed in the Péclet range considered, although for $Pe \simeq 10^2$ the first and second branches pass next to each other. The selection rule for this situation is simply [1] indicating that the first branch is dominating for all Pe values considered (i.e. up to $Pe = 10^5$).

For $\kappa = 0.6$ figure 22(b), several crossings between the real parts of the eigenvalue branches occur. The first four crossings are marked with an arrow in figure 22(b). The first crossing occurs at $Pe \simeq 6 \times 10^2$ between the first and the third branch, subsequently the third branch looses dominance and the fourth prevails. The exchange of dominance involves several other branches for increasing values of Pe so that the selection rule observed is of the form $[1 \to 3 \to 4 \to 6 \to 9 \to 11 \to \cdots]$. More regular is the exchange of dominance occurring for $\kappa = 0.8$, figure 22(c), which is characterized by the following selection rule, $[1 \to 3 \to 5 \to 7 \to 9 \to 11 \to \cdots]$.

It is important to point out that the analysis of the selection rule presented in this section is limited to the first few spectral crossings. Indeed, there is a first, partial, numerical evidence that the selection rule may be countable, i.e. that the crossings of the real part of the eigenvalues, which determine spectral dominant, form a countable cascade that persists for large Pe. This observation would explain the small amplitude oscillations observed in the localization abscissa around the mean value ρ^* predicted by the localization ansatz.

In the case of a monotonic unbounded potential, the phenomenological observation and the theoretical prediction which indicate the localization of the dominant eigenfunction at an internal point which minimizes the function $\sigma(\rho)$ must be regarded as a property stemming from the collective behaviour of eigenvalue branches more than a true asymptotic property of single branches of the spectrum.

The mathematical interpretation of the occurrence of difference selection patterns as κ increases is beyond the scope of the article, yet it represents an intriguing mathematical problem falling somewhere in between bifurcation, operator and number theory.

7. Practical relevance of the spectral approach

7.1. *Dimensionless groups and rescaling*

Consider (2.11) for given values of $\alpha = \alpha_1$, $\Gamma = \Gamma_1$ and Pe, and let $\phi^{(1)}(\xi, \mathbf{x}_\perp; \alpha_1, \Gamma_1, Pe)$ be its solution for a given inlet condition $\phi_0(\mathbf{x}_\perp)$. Let $\phi^{(2)}(\zeta, \mathbf{x}_\perp, \alpha_2, \Gamma_2, Pe)$ be the solution of the same equation for $\alpha = \alpha_2$, $\Gamma = \Gamma_2$ and Pe for the same inlet condition, and for the same operating conditions as regards both geometry (i.e. κ) and the rotation parameter Ω, i.e.

$$w(\rho)\frac{\partial \phi^{(2)}}{\partial \zeta} = -\Gamma_2\alpha_2 u(\rho)\frac{\partial \phi^{(2)}}{\partial \theta} + \frac{\alpha_2^2}{Pe}\left[\frac{1}{\rho}\frac{\partial}{\partial \rho}\left(\rho\frac{\partial \phi^{(2)}}{\partial \rho}\right) + \frac{1}{\rho^2}\frac{\partial^2 \phi^{(2)}}{\partial \theta^2}\right]. \tag{7.1}$$

By multiplying left and right-hand side of (7.1) by $(\alpha_1\Gamma_1/\alpha_2\Gamma_2)$, and defining

$$\widetilde{\zeta} = \frac{\alpha_2\Gamma_2}{\alpha_1\Gamma_1}\zeta\ , \qquad \widetilde{Pe} = Pe\,\frac{\alpha_1\Gamma_1}{\alpha_2\Gamma_2}, \tag{7.2}$$

one obtains that

$$\phi^{(2)}(\zeta, \mathbf{x}_\perp, \alpha_2, \Gamma_2, Pe) = \phi^{(1)}\left(\widetilde{\zeta}, \mathbf{x}_\perp, \alpha_1, \Gamma_1, \widetilde{Pe}\right). \tag{7.3}$$

Equation (7.3) indicates that the solution of the advection–diffusion equation for the Couette flow for given values of the aspect and velocity ratios α_2, Γ_2, respectively, is equivalent to the solution of same boundary-value problem in a Couette flow with aspect and velocity ratios α_1, Γ_1, by rescaling the axial coordinate and the Péclet number according with (7.2). This means that the results obtained for a single set of aspect and velocity ratios is fully representative of all the possible Couette flows in which both α and Γ vary arbitrarily. For $\Gamma_1 = \Gamma_2$, if $\alpha_2 \gg \alpha_1$ then the effective Péclet number $\widetilde{Pe}$ is smaller (i.e. by a factor α_1/α_2) than Pe.

A similar property applies for the spectral structure. Let $\{\lambda^{(1)}(Pe)\}$ and $\{\psi^{(1)}(\rho, Pe)\}$ be the eigenvalue and eigenfunction spectra for $\alpha = \alpha_1$, $\Gamma = \Gamma_1$ for the Couette flow in the NAD approximation, parametrized with respect to the Péclet number. The eigenvalue and eigenfunction spectra $\{\lambda^{(2)}(Pe)\}$ and $\{\psi^{(2)}(\rho, Pe)\}$ associated with a different set of aspect and velocity ratios α_2 and Γ_2 are simply given by

$$\lambda^{(2)}(Pe) = \frac{\alpha_2\Gamma_2}{\alpha_1\Gamma_1}\lambda^{(1)}\left(\widetilde{Pe}\right)\ , \qquad \psi^{(2)}(\rho, Pe) = \psi^{(1)}\left(\rho, \widetilde{Pe}\right). \tag{7.4}$$

A further observation, which is worth discussing, is related to the definition of the Péclet number. The Péclet number is defined as the ratio of the characteristic time for diffusion to the characteristic time for advection. Throughout the article we have used the definition $Pe = WL_z/\mathscr{D}$. The characteristic time for advection in an open flow tubular device is naturally associated with the axial propagation $t_{adv} = L_z/W$. For the characteristic diffusion time it is possible to choose either $t_{diff} = L_z^2/\mathscr{D}$ or $t_{diff} = R_{out}^2(1-\kappa^2)/\mathscr{D}$, since the system admits two characteristic length scales. Therefore, it is possible to introduce an alternative definition of the Péclet number, denoted with the symbol pe, with respect to the characteristic time scales of cross-sectional diffusion

$$pe = \frac{R_{out}^2(1-\kappa^2)}{\alpha^2}\,Pe. \tag{7.5}$$

For example, if $\alpha = 6$, $\kappa = 0.8$, then $pe = 10^{-2}\,Pe$ i.e. pe is a hundred times smaller that the Péclet number Pe defined with respect to $t_{diff} = L_z^2/\mathscr{D}$. Alternatively, one can define a cross-sectional Péclet number $Pe_\perp$ as $Pe_\perp = UR_{out}/\mathscr{D}$, which can be useful

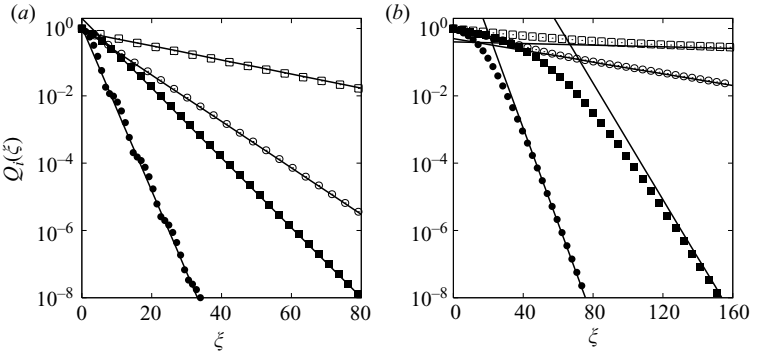

FIGURE 23. Decay of $Q_i(\xi)$ versus $\xi = \alpha \Gamma \zeta$. Dots (□) refer to $\kappa = 0.4$, $\Omega = (0, 1)$, (■) to $\kappa = 0.4$, $\Omega = (-1, 1)$, (○) to $\kappa = 0.8$, $\Omega = (0, 1)$, (●) to $\kappa = 0.8$, $\Omega = (-1, 1)$. (*a*) Refers to $Pe_o = 5.24 \times 10^2$, (*b*) refers to $Pe_o = 5.24 \times 10^4$. The solid lines are the exponential scalings $Q_{as}(\xi) = \exp(-\nu_d \xi)$ controlled by the real part of the dominant convective eigenvalue.

for simplifying some analyses, as discussed in the next paragraph. This observation on the different possible definitions of the Péclet number is relevant whenever one analyses numerical findings and experimental results obtained by different authors.

7.2. *Physical significance of the dominant eigenvalue in finite-length devices*

The spectral properties of the advection–diffusion operator can be used to describe the asymptotic behaviour of a scalar field for large values of the axial coordinate. It is therefore interesting to investigate the practical relevance of the spectral results for predicting the response of an open Couette flow device of finite length L_z.

Before addressing this issue, let us reformulate the advection–diffusion equation in the most convenient dimensionless setting. Consider (2.11), and define

$$\xi = \alpha \, \Gamma \, \zeta \, , \qquad Pe_o = \frac{Pe \Gamma}{\alpha} = \frac{U R_{out}}{\mathscr{D}}. \tag{7.6}$$

Making use of the new dimensionless variable ξ, which is no longer bounded by 1, but attains values in the range $[0, \alpha \, \Gamma]$ depending on the aspect and velocity ratios α and Γ, (2.11) becomes

$$w(\rho)\frac{\partial \phi}{\partial \xi} = -u(\rho)\frac{\partial \phi}{\partial \theta} + \frac{1}{Pe_o}\left[\frac{1}{\rho}\frac{\partial}{\partial \rho}\left(\rho \frac{\partial \phi}{\partial \rho}\right) + \frac{1}{\rho^2}\frac{\partial^2 \phi}{\partial \theta^2}\right], \tag{7.7}$$

which is suitable for a general comparison of the spectral results with the performance of a finite-length Couette flow device. Let $\widetilde{\lambda} = \lambda / \alpha \Gamma = \nu + i\widetilde{q}$ be the eigenvalues associated with normalized (7.7).

As a reference quantity we consider the weighted cross-sectional L^2-norm $Q_i(\xi) = [\int_{S_\perp} w(\rho)\,(\phi(\mathbf{x}_\perp, \xi) - \overline{\phi})^2 \, \mathrm{d}\mathbf{x}_\perp]^{1/2}$, where $\overline{\phi}$ is the cross-sectional average, and compare the axial decay of $Q_i(\xi)$ with the exponential scaling $Q_{as}(\xi) = C\mathrm{e}^{-\nu_d \xi}$ associated with the dominant convective eigenvalue. The constant C is a parameter that can be obtained by fitting the exponential asymptotic decay of $Q_i(\xi)$. The inlet condition $\phi_{in}(\rho, \theta)$ is the same used in § 2.4.

The comparison of $Q_i(\xi)$ and $Q_{as}(\xi)$ is depicted in figure 23, for two different values of Pe_o equal to 5.24×10^2 (figure 23*a*) and 5.24×10^4 (figure 23*b*) for several flow conditions. At intermediate values of $Pe_o \simeq 5 \times 10^2$ (figure 23*a*), the dominant convective scaling is representative for the advection–diffusion dynamics starting from values of $\xi \simeq 10$. As Pe_o increases, the asymptotic exponential scaling sets in for higher

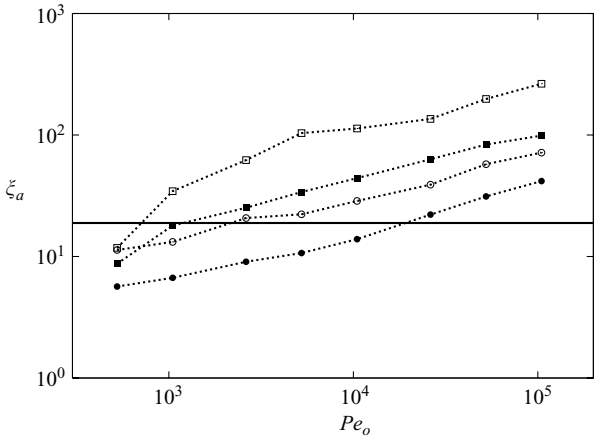

FIGURE 24. ξ_a versus Pe_o for several open Couette flows. (□) $\kappa = 0.4$, $\Omega = (0, 1)$, (■) $\kappa = 0.4$, $\Omega = (-1, 1)$, (○) $\kappa = 0.8$, $\Omega = (0, 1)$, (●) $\kappa = 0.8$, $\Omega = (-1, 1)$. The solid horizontal line corresponds to $\zeta = 1$ for $\alpha = 6$, $\Gamma = \pi$.

values of ξ, and the assessment of the asymptotic exponential scaling becomes more dependent on the operating conditions (compare the cases $\kappa = 0.4$, $\Omega = (0, 1)$ and $\kappa = 0.8$, $\Omega = (-1, 1)$ in figure 23 *b*).

A quantitative indicator of the setting of the asymptotic conditions can be formulated by introducing a critical asymptotic abscissa ξ_a, defined as the lower value of ξ for which $|Q_i(\xi) - Q_{as}(\xi)| < \eta$, for $\xi > \xi_a$, where η is a small parameter. We choose $\eta = 10^{-2}$. Given ξ_a, it is possible to establish the values of the aspect and velocity ratios α and Γ at which the asymptotic exponential scaling becomes physically relevant in a finite-length device.

Recalling the definition of the normalized abscissa ξ equation (7.6), and assuming that the assessment of the asymptotic scaling sets in at the outlet of the device, one obtains $\xi_a = (\alpha \Gamma \zeta)_a|_{\zeta=1}$. Given Γ and ξ_a for the specific operating conditions, one can recover the minimum aspect ratio $\alpha_a = \xi_a/\Gamma$, starting from which the asymptotic decay and the dominant eigenfunction control the structure of the outlet concentration profile. An analogous result can be obtained by fixing α and varying Γ.

Figure 24 shows the value of the critical asymptotic abscissa ξ_a for the four operating conditions analysed throughout the article as a function of Pe_o. The value of ξ_a increases monotonically with Pe and is higher for smaller internal radii, and when the inner cylinder is static $\Omega = (0, 1)$. It is possible to use the data depicted in figure 24 in order to determine the critical value of Pe_o, for fixed values of α and Γ. For example, consider $\alpha = 6$, $\Gamma = \pi$, and draw the horizontal line $\xi^* = \alpha\Gamma$ (depicted in figure 24). All the values of Pe_o such that $\xi_a(Pe_o) < \xi^*$ corresponds to flow conditions for which the asymptotic scaling rapidly sets in within the flow device.

To give an example, figure 25 shows the spatial structure of the (normalized) concentration profile at $\theta = \pi/3$ for $\alpha = 6$, $\Gamma = \pi$, $\kappa = 0.8$, $\Omega = (-1, 1)$ for the same inlet condition used for the simulations depicted in figure 23, for values of Pe_o slightly lower than (figure 25*a*), and slightly above (figure 25*b*) the value Pe_o^*, defined by $\xi_a(Pe_o^*) = \alpha\Gamma$. In both cases, the outlet profile converges rapidly towards a spatial pattern close to the profile of the dominant convection-enhanced eigenfunction (not shown for the sake of brevity). This example indicates that the criterion chosen for

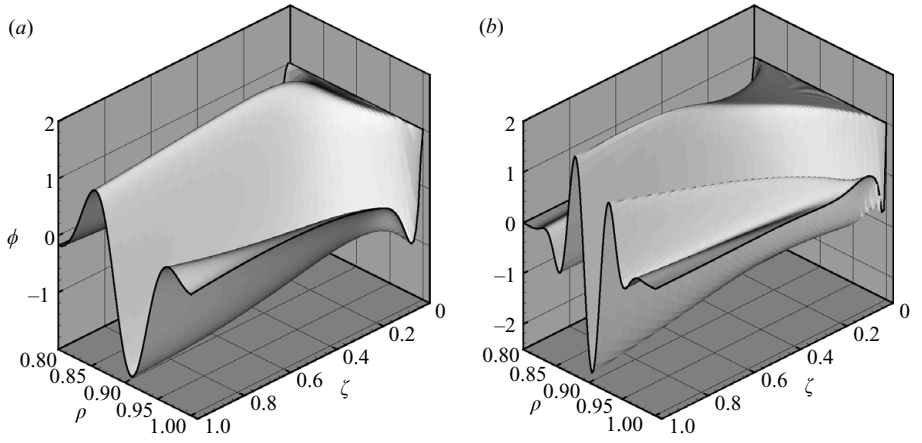

FIGURE 25. Normalized spatial profile of the concentration ϕ along a Couette channel $\kappa = 0.8$ ($\alpha = 6$, $\Gamma = \pi$), $\Omega = (-1, 1)$ as a function of ρ and ζ at $\theta = \pi/3$ starting from a segregated inlet. (*a*) $Pe_o = 5.24 \times 10^3$. (*b*) $Pe_o = 5.24 \times 10^4$.

ξ_a is very strict for assessing the achievement of asymptotic conditions at the outlet section.

As a final comment, it is worth observing that the range of Péclet numbers, aspect ratios, and operating conditions associated with realistic microflow devices gives rise to values of $Pe_o < 10^5$, and values of the group $(\alpha\Gamma)$ in the range $[10^0, 10^2]$ (Nguyen & Wu 2005; Nguyen & Wereley 2006), which correspond to the ranges of values considered in figure 25.

8. Concluding remarks

In this article we studied the mixing properties of a typical, physically realizable open flow system, the open Couette flow under creeping conditions. The NAD approximation, which can be assumed valid for $Pe > Pe^*$ (where $Pe^* \simeq 5 \times 10^2$ for $\alpha = 6$, $\Gamma = \pi$) permits to approach the characterization of mixing regimes in the form of a generalized eigenvalue problem. The spectral approach provides a way to characterize mixing in finite-length devices provided that the aspect ratio is sufficiently large.

The open Couette flow exhibits a rich spectral behaviour which depends on the geometry (i.e. on the ratio κ of the two cylinder radii) and on the parameter Ω expressing the relative rotation of the inner and outer cylinders. For $\Omega = (0, 1)$, the asymptotic evolution of passive scalar fields displays a spectral phase-transition which is controlled by the geometric parameter κ. The spectral phase transition influences the localization abscissa $\rho^*(\kappa)$ of the dominant eigenfunctions and the scaling exponent γ. This transition is continuous with respect to the order parameter $\rho^*(\kappa)$, but displays a discontinuity in the scaling exponent γ which attains the value $\gamma = 1/2$ for $\kappa < \kappa_c$ and $\gamma = 1/4$ for $\kappa > \kappa_c$.

The properties of the asymptotic mixing regimes depend on the form of the effective potential $V_{eff}(\rho)$ and of the dimensionless axial velocity $w(\rho)$. The localization ansatz formulated in § 5 provides an explanation of the localization properties of the eigenfunctions, and has been justified analytically in the case $V_{eff}(\rho)$ is a monotonic function of its argument, diverging at the solid walls. The use of norm equalities (3.5), (3.8) and eigenfunction invariance (3.11) is a simple and powerful tool to predict the scaling exponent γ for large Péclet values.

The rotation condition $\Omega = (-1, 1)$ is particularly interesting both from the theoretical and the practical point of view. The spectral structure of the advection–diffusion operator for $\Omega = (-1, 1)$ is characterized by the occurrence of four regimes as Pe increases: (i) a diffusional regime controlled by the action of the Laplacian operator along the angular coordinate θ, (ii) a Neumann regime which can be viewed as a perturbation of the uniform conditions, (iii) an intermediate regime at which the real part of the eigenvalue is practically independent of Pe and (iv) an asymptotic regime characterized by the eigenvalue scaling $-\mu_d \sim Pe^{-1/3}$.

The intermediate and asymptotic regimes unveils a complex spectral structure characterized by the interaction between spectral branches giving rise to branch crossing and exchange of dominance. The phenomenon of crossing of the real parts associated with single spectral branches crossing is, to the best of our knowledge, a new spectral phenomenon in connection with non-Hermitian operators of fluid dynamic interest.

The region of intermediate Péclet values is also interesting for practical purposes. The almost constant scaling of $-\mu_d$ versus Pe corresponds to optimal mixing conditions. The range of Péclet values corresponding to these optimal conditions spans more that two decades (two decades in Pe means that the same decay exponent $-\mu_d$ characterizes the length scale of homogenization for stationary mixing of small organic molecules, such as small vitamins and that of large globular proteins), and corresponds to the typical range of operation of micromixing systems (Nguyen & Wu 2005; Nguyen & Wereley 2006).

It is important to point out that the rich spectral behaviour characterizing the open Couette flow is intrinsically related to the interplay between the angular and axial components of the velocity field and diffusion. For $w(\rho) = 1$, i.e. in the plug flow case, none of spectral phenomena occurs, and the system behaves as an equivalent closed system. The presence of a non-uniform axial profile $w(\rho)$, which physically corresponds to a laminar open flow in the presence of no-slip boundary conditions, is the ultimate cause of the rich spectral properties found in this system.

To sum up, the case study of the open Couette flow developed in this article represents, to the best of our knowledge, one of the first systematic analyses of mixing in an open flow device, and indicates that the open Couette system can be considered as a prototypical example of a continuous mixer operating mixer in the laminar regime associated with non-chaotic kinematics. The topics covered in this article span all the main properties of this system. Minor, yet not less important, issues will be object of future investigation. For instance, a problem that has not been addressed is the spectral invariance as a function of Pe, which characterizes the plug flow case (see figure 4).

This article focused on the stationary mixing properties of the Couette flow system. Future work will address its transient (dynamic) properties and the spectral properties of other prototypical models of open microflow devices, which can be tackled with the same techniques used in the present article. Although the approach followed in this article is suited for simple flows, and cannot be extended straightforwardly to time periodic velocity fields giving rise to partially chaotic kinematics, localization concepts could be used for attempting a quantitative prediction of the mixing regimes and homogenization exponents also for partially chaotic flows characterized by the occurrence of regions of kinematic regular motion, intermingled with invariant chaotic ergodic subsets (Giona *et al.* 2004*a*).

Appendix A. Simulation details

Let us first consider the NAD approximation. For fixed m, the solution of (3.2) can be approached by means of a Galerkin expansion with respect to a basis of square summable function $\{c_n(\rho)\}_{n=0}^{\infty}$ in the interval $(\kappa, 1)$, and satisfying the Neumann boundary conditions at $\rho=\kappa, 1$, i.e. $\mathrm{d}c_n(\rho)/\mathrm{d}\rho|_{\rho=\kappa,1}=0$,

$$\phi_m(\zeta, \rho) = \sum_{n=0}^{\infty} \phi_{m,n}(\zeta)\, c_n(\rho). \tag{A 1}$$

Specifically, we chose the cosine basis

$$c_n(\rho) = \cos\left[n\pi \frac{(\rho-\kappa)}{(1-\kappa)}\right], \qquad n=0, 1, \ldots, \tag{A 2}$$

which is orthogonal in $(\kappa, 1)$, i.e. $\int_{\kappa}^{1} c_n(\rho)\, c_k(\rho)\, \mathrm{d}\rho = \sigma_n^2 \delta_{n,k}$, where $\delta_{n,k}$ are the Kronecker symbols and $\sigma_0=(1-\kappa)$, $\sigma_n=(1-\kappa)/2$, $n=1, 2, \ldots$. For fixed m, let us truncate the expansion equation (A 1) up to $N+1$ modes, i.e. $n=0, \ldots, N$. Let $\boldsymbol{\phi}=(\phi_{m,0}, \ldots, \phi_{m,N})^T$ be the vector of the truncated Fourier coefficients. Equation (3.2) can be recast in matrix form for the coefficient vector $\boldsymbol{\phi}$ as

$$\mathbf{B}\frac{\partial \boldsymbol{\phi}}{\partial \zeta} = -i\boldsymbol{A}\,\boldsymbol{\phi} + \varepsilon_{\alpha}\mathbf{C}\boldsymbol{\phi} = \mathscr{M}_{\varepsilon_{\alpha}}\,\boldsymbol{\phi}, \tag{A 3}$$

where the imaginary matrix $i\boldsymbol{A}$ expresses the action of the cross-sectional advection ($\mathbf{A}=(A_{n,k})$), $\mathbf{B}=(B_{n,k})$ the influence of the axial flow, and $\varepsilon_{\alpha}\mathbf{C}$ the action of cross-sectional diffusion ($\mathbf{C}=(C_{n,k})$):

$$A_{n,k} = m\Gamma\alpha \int_{\kappa}^{1} u(\rho)\, c_n(\rho)\, c_k(\rho)\, \mathrm{d}\rho\,, \qquad B_{n,k} = \int_{\kappa}^{1} w(\rho)\, c_n(\rho)\, c_k(\rho)\, \mathrm{d}\rho, \tag{A 4}$$

$$C_{n,k} = \left[\int_{\kappa}^{1} c_n(\rho)\, \frac{1}{\rho}\, \frac{\mathrm{d}}{\mathrm{d}\rho}\left(\rho\, \frac{\mathrm{d}c_k(\rho)}{\mathrm{d}\rho}\right) \mathrm{d}\rho - m^2 \int_{\kappa}^{1} \frac{1}{\rho^2}\, c_n(\rho)\, c_k(\rho)\, \mathrm{d}\rho\right]. \tag{A 5}$$

The numerical issues associated with (A 3) refer to the simulation of (A 3) and to the estimate of its spectral (eigenvalue/eigenvector) properties. Let us discuss these two aspects separately.

The numerical simulation of (A 3) is performed by applying an implicit finite-difference scheme along the ζ-coordinate. Let $\{\zeta_i\}$ be an equally spaced grid along the ζ coordinate, $\zeta_{i+1}-\zeta_i=\Delta\zeta$, and let $\boldsymbol{\phi}_{\zeta_i}$ be the value of the vector-valued function $\boldsymbol{\phi}$ at $\zeta=\zeta_i$. Discretizing (A 3) via an implicit finite-difference scheme, one obtains $\mathbf{B}\boldsymbol{\phi}_{\zeta_i+\Delta\zeta} - \mathbf{B}\boldsymbol{\phi}_{\zeta_i} = \mathbf{M}_{\varepsilon_{\alpha}}\,\Delta\zeta\,\boldsymbol{\phi}_{\zeta_i+\Delta\zeta}$, from which it follows that

$$\boldsymbol{\phi}_{\zeta_i+\Delta\zeta} = \left(\mathbf{B} - \Delta\zeta\,\mathbf{M}_{\varepsilon_{\alpha}}\right)^{-1}\mathbf{B}\,\boldsymbol{\phi}_{\zeta_i}. \tag{A 6}$$

The numerical scheme equation (A 6) applies to the NAD approximation starting from the value of the vector-valued function $\boldsymbol{\phi}_{\zeta_0=0}$ at the inlet.

In the general case, i.e. when axial diffusion is accounted for, the solution of the complete equation (2.11) can be easily obtained by adopting a relaxation method applied to an operator-splitting algorithm, in which first the model is solved in the absence of axial diffusion for a given time step, and subsequently, a pure diffusion equation along the axial direction is advanced for the same time-step.

Let us consider these two steps separately. The first step in the operator-splitting strategy involves the NAD approximation. In matrix form, the time-dependent

formulation of the NAD approximation reads

$$\frac{\partial \boldsymbol{\phi}}{\partial \tau} + \mathbf{B}\,\frac{\partial \boldsymbol{\phi}}{\partial \zeta} = \mathbf{M}_{\varepsilon_\alpha}\,\boldsymbol{\phi}, \tag{A 7}$$

where the dimensionless time τ is $\tau = tW/L_z$. Let $\boldsymbol{\phi}^{\tau}_{\zeta_i}$ be the discretized vector-valued function of the Fourier coefficients at the axial position ζ_i and time τ. Equation (A 7) can been approached numerically by means of an implicit algorithm:

$$\widetilde{\boldsymbol{\phi}}^{\tau+\Delta\tau}_{\zeta_i+\Delta\zeta} = \left[\mathbf{I} - \Delta\tau\,\mathbf{M}_{\varepsilon_\alpha}\right]^{-1}\left[\boldsymbol{\phi}^{\tau}_{\zeta_i+\Delta\zeta} + \delta\mathbf{B}\left(\boldsymbol{\phi}^{\tau}_{\zeta_i+\Delta\zeta} - \boldsymbol{\phi}^{\tau}_{\zeta_i}\right)\right], \tag{A 8}$$

where $\delta = \Delta\tau/\Delta\zeta < 1$ ($\delta = 0.1$). For a fixed $\Delta\tau$, the second step of the algorithm involves pure diffusion along the axial coordinate. Letting $\widehat{\boldsymbol{\phi}}^{\tau}_{\zeta_i} = \widetilde{\boldsymbol{\phi}}^{\tau+\Delta\tau}_{\zeta_i}$ be the starting concentration field obtained at the previous step, the vector-valued function expressing the concentration field at time $t+\Delta\tau$ is obtained by solving explicitly the pure diffusion equation

$$\widehat{\boldsymbol{\phi}}^{\tau+h_\tau}_{\zeta_i} = \widehat{\boldsymbol{\phi}}^{\tau}_{\zeta_i} + \frac{h_\tau}{Pe(\Delta\zeta)^2}\left(\widehat{\boldsymbol{\phi}}^{\tau}_{\zeta_i+\Delta\zeta} + \widehat{\boldsymbol{\phi}}^{\tau}_{\zeta_i-\Delta\zeta} - 2\,\widehat{\boldsymbol{\phi}}^{\tau}_{\zeta_i}\right) \tag{A 9}$$

for a time interval equal to $\Delta\tau$. Here h_τ is the time interval for the integration of the diffusive step, which fulfils the stability constraint $h_\tau < 0.5Pe(\Delta\zeta)^2$. Since, in general, $h_\tau < \Delta\tau$, this implies that (A 9) is iterated N_d-times where $N_d = \Delta\tau/h_\tau$ (in practice h_τ is chosen to fulfil the stability constraint, and such that the ratio $\Delta\tau/h_\tau$ returns an integer). The value of the coefficient vector at time $\tau + \Delta\tau$ is thus $\boldsymbol{\phi}^{\tau+\Delta\tau}_{\zeta_i} = \widehat{\boldsymbol{\phi}}^{\tau+N_d h_\tau}_{\zeta_i}$. This operator-splitting procedure is iterated until stationary conditions are reached.

The discretized solution of the advection–diffusion equation depends on the number of modes ($2M+1$, i.e. $|m| \leqslant M$) along θ, and ρ (which are $N+1$, i.e. $n = 0, 1, \ldots, N$), and on the step size $\Delta\zeta$ along the axial coordinate. The choice of the appropriate values for these quantities (i.e. M, N and $\Delta\zeta$) for a fixed accuracy depends on the value of the Péclet number. In the simulations, the values for M, N and $\Delta\zeta$ have been selected according to a heuristic (*ex-post*) criterion, as the values for which the solutions were close (according to a prescribed accuracy) to the solutions obtained by doubling the modes (i.e. taking $2M$, and $2N$) and reducing by half the axial step size (i.e. taking $\Delta\zeta/2$). In practice, $M, N = 30$, 60 and $\Delta\zeta = 10^{-3}$ for $Pe \leqslant 10^3$, while $M, N = 120$ up to 480 (depending on the operating conditions), and $\Delta\zeta = 10^{-4}$ for $Pe \simeq 10^6$.

As it regards spectral analysis, the spectrum of the advection–diffusion operator in the NAD approximation (3.2) is defined by the equation

$$\lambda\, w(\rho)\,\psi(\rho) = -im\Gamma\alpha u(\rho)\,\psi(\rho) + \varepsilon_\alpha\left[\frac{1}{\rho}\,\frac{\partial}{\partial\rho}\left(\rho\,\frac{\partial\psi(\rho)}{\partial\rho}\right) - \frac{m^2}{\rho^2}\,\psi(\rho)\right], \qquad m \in \mathbb{N}, \tag{A 10}$$

where $\lambda \in \mathbb{C}$ is the eigenvalue and ψ the corresponding eigenfunction.

Numerically, this problem trasforms into a generalized eigenvalue problem associated with (A 3):

$$\lambda\,\boldsymbol{B}\,\boldsymbol{\psi} = \boldsymbol{M}_{\varepsilon_\alpha}\,\boldsymbol{\psi}. \tag{A 11}$$

Equation (A 11) has been solved by applying two different routines: the QR algorithm to the matrix $\boldsymbol{B}^{-1}\boldsymbol{M}_{\varepsilon_\alpha}$ by first reducing this matrix into an upper Hessemberg form, and the EISPACK routine `rgg` which approaches directly the generalized eigenvalue problem. For fixed m, the truncated modal representation (A 11) depends on N, i.e. on the number $(N+1)$ of radial modes. The appropriate choice of N

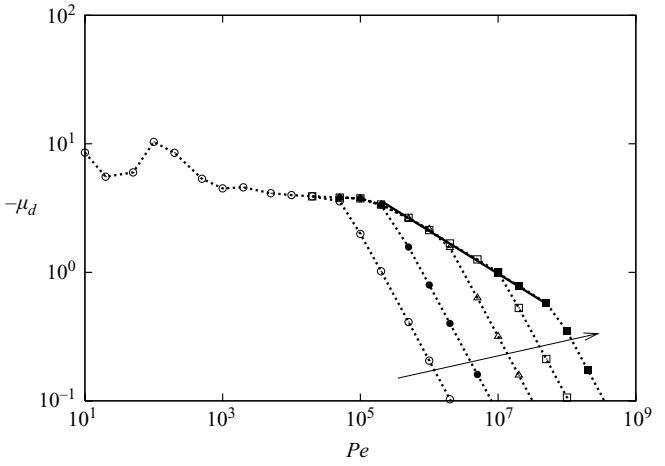

FIGURE 26. Real part of the dominant eigenvalue μ_d versus Pe for the Couette flow $\kappa = 0.4$, $\Omega = (-1, 1)$. The arrow indicates increasing modal resolution in the numerical truncation, starting from $N = 30$ (○), $N = 60$ (●), $N = 120$ (△), $N = 220$ (□), up to $N = 400$ (■).

depends on the Pe value, so that the value of N has be chosen case by case in order to ensure a prescribed accuracy.

To give an example, figure 26 depicts the behaviour of the real part μ_d ($\lambda_d = \mu_d + iq_d$) of dominant eigenvalue as a function of Pe for $m = 1$ for the Couette flow $\kappa = 0.4$, $\Omega = (-1, 1)$, i.e. when the two cylinders counter-rotate, for different truncations of the modal expansion. While for $Pe \leqslant 10^4$, $N = 30$ is fully sufficient to obtain a reliable numerical result, at least $N = 400$ modes are required for $Pe \simeq 10^7$. While the detailed analysis of the scaling of μ_d with Pe is addressed in the main body of the article, it can be observed that truncation effects, when the modal resolution is insufficient, appear as a spurious diffusional scaling $-\mu_d \sim Pe^{-1}$ (the family of parallel lines in figure 26 crossed by the arrow), which disappears as the modal resolution is increased. Similar behaviours are observed for the other flow conditions analysed in this article.

Appendix B. Scaling calculations for the dominant eigenvalue

By enforcing the localization ansatz, and the invariance property of the dominant convection-enhanced eigenfunction expressed by (3.11), it is possible to obtain analytically the dependence of the scaling exponent γ on the flow conditions. The technique used is identical to the derivation developed in § 3.3 for the Couette plug flow. Since (3.5) is a basic ingredient to derive the asymptotic scaling, it is useful to rewrite it in a more compact form. Let

$$\left.\begin{aligned} \langle \psi_d, w \rangle &= \int_0^1 \rho w(\rho)\, \psi_d(\rho)\, \mathrm{d}\rho = G_{w,R} + i\, G_{w,I}, \\ \langle \psi_d, V \rangle &= \int_0^1 \rho V(\rho)\, \psi_d(\rho)\, \mathrm{d}\rho = G_{V,R} + i\, G_{V,I}. \end{aligned}\right\} \tag{B 1}$$

By solving (3.5) for the real part μ_d of the eigenvalue, one obtains

$$-\mu_d = \frac{\left(G_{V,I}\, G_{w,R} - G_{V,R} G_{w,I}\right)}{(G_{w,R})^2 + (G_{w,I})^2}. \tag{B 2}$$

Consider first the condition for which the localization occurs at the inner cylinder radius $\rho^* = \kappa$, as e.g. for $\kappa = 0.8$, $\Omega = (0, 1)$. In a neighbourhood of ρ^*, $V(\rho)$ and $w(\rho)$ admit the following series expansion:

$$V(\rho) = V_1(\rho-\kappa)+V_2(\rho-\kappa)^2+O(|\rho-\kappa|^3), \quad w(\rho) = w_1(\rho-\kappa)+w_2(\rho-\kappa)^2+O(|\rho-\kappa|^3), \tag{B 3}$$

where V_h, w_h $h = 1, 2$ are constant. Making use of the invariance equation (3.11), and introducing the auxiliary integration variable ξ defined as $\rho = \kappa + \xi\,\beta(\varepsilon_\alpha)$, the norm $||\psi_d||_w^2$ can be expressed as

$$||\psi_d||_w^2 = \int_\kappa^1 \rho\, w(\rho)\, |\psi_d|^2(\rho)\, \mathrm{d}\rho = A^2(\varepsilon_\alpha)\beta^2(\varepsilon_\alpha) w_1 \kappa C_1 + O(\beta^3) \quad C_1 = \int_0^\infty \xi\, |\psi_{d,i}(\xi)|^2\, \mathrm{d}\xi. \tag{B 4}$$

The upper integration limit in the definition of the constant C_1 is set to ∞ since, for large Pe, $(1-\kappa)/\beta(\varepsilon_\alpha) \to \infty$. Similarly,

$$||\partial_\rho \psi_d||_{L^2}^2 = \int_\kappa^1 \rho \left|\frac{\partial \psi_d(\rho)}{\partial \rho}\right|^2 \mathrm{d}\rho = \frac{A(\varepsilon_\alpha)^2\,\kappa}{\beta(\varepsilon_\alpha)}\,(D_0 + O(\beta)), \quad D_0 = \int_0^\infty \left|\frac{\partial \psi_{d,i}(\xi)}{\partial \xi}\right|^2 \mathrm{d}\xi, \tag{B 5}$$

$$||\psi/\rho||_{L^2}^2 = \int_\kappa^1 \frac{1}{\rho}\, |\psi_d(\rho)|^2\, \mathrm{d}\rho = \frac{A^2(\varepsilon_\alpha)\beta(\varepsilon_\alpha)}{\kappa} C_0 + O\left(\beta^2\right), \qquad C_0 = \int_0^\infty |\psi_{d,i}(\xi)|^2\, \mathrm{d}\xi. \tag{B 6}$$

Gathering (B 4)–(B 6), and substituting them into (3.8), one obtains

$$-\mu_d \sim \frac{\varepsilon_\alpha D_0}{w_1 C_1} \frac{1}{\beta^3(\varepsilon_\alpha)} + O\left(\beta^{-2}\right) = \frac{K_0\,\varepsilon_\alpha}{\beta^3(\varepsilon_\alpha)} + O\left(\beta^{-2}\right), \tag{B 7}$$

where $K_0 = D_0/w_1 C_1$. Consider now (B 2). From the local expansion (B 3), it follows that

$$G_w = \int_\kappa^1 \rho\, \left[w_1(\rho-\kappa) + O\left(|\rho-\kappa|^2\right)\right]\, \psi_d(\rho)\, \mathrm{d}\rho = A(\varepsilon_\alpha)\kappa w_1 \beta^2(\varepsilon_\alpha) G^1 + O\left(\beta^3\right), \tag{B 8}$$

where $G^h = \int_0^\infty \xi^h\, \psi_{d,i}(\xi)\mathrm{d}\xi = G_R^h + i G_I^h$, $h = 0, 1, 2, \ldots$. Therefore, the denominator of (B 2) reads

$$(G_{w,R})^2 + (G_{w,I})^2 = A^2(\varepsilon_\alpha)\kappa^2 w_1^2 \beta^4(\varepsilon_\alpha)\, \left[\left(G_R^1\right)^2 + \left(G_I^1\right)^2\right] + O\left(\beta^6\right). \tag{B 9}$$

For estimating the numerator of (B 2), it is convenient to observe that the potential $V(\rho)$ in the neighbourhood of the localization abscissa $\rho = \kappa$ can be expressed as a function of $w(\rho)$ as

$$\frac{V(\rho)}{w(\rho)} = a_0 + a_1(\rho-\kappa) + O(|\rho-\kappa|^2). \tag{B 10}$$

Therefore,

$$\begin{aligned} G_V &= a_0 G_w + a_1 w_1 \int_\kappa^1 \rho\,(\rho-\kappa)^2\, \psi_d(\rho)\, \mathrm{d}\rho + \int_\kappa^1 \rho\, O(|\rho-\kappa|^3)\, \psi_d(\rho)\, \mathrm{d}\rho \\ &= a_0 G_w + A(\varepsilon_\alpha) a_1 w_1 \kappa \beta^3(\varepsilon_\alpha)\, G^2 + O(\beta^4). \end{aligned} \tag{B 11}$$

This leads to the following expression for the numerator of (B 2):

$$G_{V,I} G_{w,R} - G_{V,R} G_{w,I} = A^2(\varepsilon_\alpha) a_1 w_1^2 \kappa^2 \beta^5(\varepsilon_\alpha)\, \left(G_I^2 G_R^1 - G_R^2 G_I^1\right) + O\left(\beta^6\right). \tag{B 12}$$

Substituting (B 9), (B 12) into (B 2) one obtains

$$-\mu_d = K_1\beta + O\left(\beta^2\right), \tag{B 13}$$

where $K_1 = a_1(G_I^2 G_R^1 - G_R^2 G_I^1)$. From (B 7), (B 13), the following expression for $\beta(\varepsilon_\alpha)$ is obtained to the leading order

$$\beta(\varepsilon_\alpha) = \left(\frac{K_0}{K_1}\right)^{1/4} \varepsilon_\alpha^{1/4}, \tag{B 14}$$

which provides for $-\mu_d$ the scaling law

$$-\mu_d = K_1 \left(\frac{K_0}{K_1}\right)^{1/4} \varepsilon_\alpha^{1/4} \sim Pe^{-1/4}. \tag{B 15}$$

This result is in agreement with the value $\gamma = 1/4$ found for $\kappa = 0.8$, $\Omega = (0, 1)$.

Consider now the case $\kappa = 0.4$, $\Omega = (0, 1)$, which is characterized by the occurrence of a local quadratic minimum at an internal radial abscissa ρ^*. The function $w(\rho)$ and $V_{eff}(\rho)$ close to ρ^* can be expanded in Taylor series as

$$w(\rho) = w_0 + w_1(\rho - \rho^*) + O\left(|\rho - \rho^*|^2\right), \tag{B 16}$$

$$V_{eff}(\rho) = \frac{V(\rho)}{w(\rho)} = a_0 + a_2(\rho - \rho^*)^2 + O\left(|\rho - \rho^*|^3\right). \tag{B 17}$$

In this case one obtains

$$\left.\begin{aligned} ||\psi_d||_w^2 &= A^2(\varepsilon_\alpha)\beta(\varepsilon_\alpha) w_0 \kappa C_0 + O(\beta^2), \qquad C_0 = \int_{-\infty}^{\infty} |\psi_{d,i}(\xi)|^2 \,\mathrm{d}\xi \\ ||\partial_\rho \psi_d||_{L^2}^2 &= \frac{A^2(\varepsilon_\alpha)\kappa}{\beta} D_0 + O(1)\,, \qquad D_0 = \int_{-\infty}^{\infty} |\partial_\xi \psi_{d,i}|^2 \,\mathrm{d}\xi \\ ||\psi_d/\rho||_{L^2}^2 &= \frac{A^2(\varepsilon_\alpha)\beta(\varepsilon_\alpha)}{\kappa} C_0 + O(\beta^2). \end{aligned}\right\} \tag{B 18}$$

The difference with respect to the previous case is that now $w(\rho)$ is, to the leading order, constant in a neighbourhood of the localization abscissa, whereas in the previous case the leading order of $w(\rho)$ close to ρ^* was linear. The different local behaviour of $w(\rho)$ near ρ implies a different scaling of $||\psi_d||_w^2$ with $\beta(\varepsilon_\alpha)$ in the two cases. Since ρ^* is an internal point, the lower and upper integration limits are now $\pm\infty$ since for $\varepsilon_\alpha \to 0$ $(\kappa - \rho^*)/\beta(\varepsilon_\alpha) \to -\infty$, and $(1 - \rho^*)/\beta(\varepsilon_\alpha) \to \infty$. The substitution of the expressions for the norms of (B 18) entering (3.8) provides

$$-\mu_d = \frac{K_0\,\varepsilon_\alpha}{\beta^2(\varepsilon_\alpha)} + O(\beta^{-1}). \tag{B 19}$$

For deriving the expression at the right-hand side of (B 2), it is sufficient to observe that $O(1)$ is the leading order for $w(\rho)$ close to ρ^*. This implies for the denominator of (B 2):

$$(G_{w,R})^2 + (G_{w,I})^2 = A^2(\varepsilon_\alpha)\kappa^2 w_0^2 \beta^2(\varepsilon_\alpha) \left[(G_R^0)^2 + (G_I^0)^2\right] + O\left(\beta^4\right). \tag{B 20}$$

For G_w one obtains

$$G_w = A(\varepsilon_\alpha) w_0 \kappa \beta(\varepsilon_\alpha) G^0 + O(\beta^2). \tag{B 21}$$

The expression of G_V can be obtained by enforcing (B 17), namely the fact that $V(\rho)$ is proportional to $w(\rho)$ close to ρ^* plus a quadratic contribution. This yields

$$G_V = a_0 G_w + a_2 w_0 \int_\kappa^1 \rho\,(\rho-\rho^*)^2\,\psi_d(\rho)\,\mathrm{d}\rho + \int_\kappa^1 \rho\,O(|\rho-\rho^*|^3)\,\psi_d(\rho)\,\mathrm{d}\rho$$
$$= a_0 G_w + a_2 A(\varepsilon_\alpha) w_0 \kappa \beta^3(\varepsilon_\alpha) G^2 + O(\beta^4). \tag{B 22}$$

Observe that all the quantities G^h, $h=0,1,2$ introduced are identical to the corresponding quantities defined in the previous case, with the only difference that now the lower integration limit is $-\infty$ instead of 0. Equations (B 21)–(B 22) provide for the numerator of (B 2) the following expression:

$$G_{V,I} G_{w,R} - G_{V,R} G_{w,I} = A^2(\varepsilon_\alpha) a_2 w_0^2 \kappa^2 \beta^4(\varepsilon_\alpha)\left(G_I^2 G_R^0 - G_R^2 G_I^0\right) + O(\beta^5). \tag{B 23}$$

Consequently, (B 2) returns the following relation between μ_d and $\beta(\varepsilon_\alpha)$:

$$-\mu_d = K_1 \beta^2(\varepsilon_\alpha) + O(\beta^3), \tag{B 24}$$

where $K_1 = a_2(G_I^2 G_R^0 - G_R^2 G_I^0)$. From (B 19) and (B 24), $\beta(\varepsilon_\alpha)$ can be expressed, to the leading order, as a function of ε_α for $\varepsilon_\alpha \to 0$ as

$$\beta(\varepsilon_\alpha) = \left(\frac{K_0}{K_1}\right)^{1/4} \varepsilon_\alpha^{1/4} \tag{B 25}$$

and, via (B 24), the asymptotic scaling of μ_d versus ε_α is derived:

$$-\mu_d = K_1 \left(\frac{K_0}{K_1}\right)^{1/2} \varepsilon_\alpha^{1/2} \sim Pe^{-1/2}. \tag{B 26}$$

Equation (B 26) predicts the asymptotic scaling exponent $\gamma = 1/2$ found for $\kappa = 0.4$, $\Omega = (0, 1)$.

Let us next analyse the last situation observed in the open Couette flow, corresponding to the rotation condition $\Omega = (-1, 1)$, for which $V_{eff}(\rho)$ is a monotonically increasing function of ρ, diverging to $\pm\infty$ in the near-wall regions. In this case the localization ansatz predicts that eigenfunction localization occurs at an internal point ρ^*. Close to the localization point ρ^*, the functions Close to the localization point ρ^*, the functions $w(\rho)$ and $V(\rho)$ behaves as

$$w(\rho) = w_0 + w_1(\rho-\rho^*) + O(|\rho-\rho^*|^2), \tag{B 27}$$

$$V_{eff}(\rho) = \frac{V(\rho)}{w(\rho)} = a_0 + a_1(\rho-\rho^*) + O(|\rho-\rho^*|^2). \tag{B 28}$$

Observe that the local behaviour of $w(\rho)$ is identical to the previous case $\kappa = 0.4$, $\Omega = (0, 1)$. The main difference with respect to that operating condition is that now $V_{eff}(\rho)$ is locally linear (and not quadratic) close to ρ^*. From this observation it follows that the norm estimates for $||\psi_d||_w^2$, $||\partial_\rho \psi||_{L^2}^2$ and $||\psi/\rho||_{L^2}^2$ are still given by (B 18), and consequently (B 19) holds for $-\mu_d$. The expressions (B 27)–(B 28) substituted into the integrals entering (B 2) lead to the following alternative equation for μ_d (we omit all the algebraic manipulations which are substantially identical to the previous case):

$$-\mu_d = K_1 \beta(\varepsilon_\alpha) + O(\beta^2), \tag{B 29}$$

where $K_1 = a_1(G_I^1 G_R^0 - G_R^1 G_I^0)$. From (B 18), (B 29), it follows that

$$\beta(\varepsilon_\alpha) = \left(\frac{K_0}{K_1}\right)^{1/3} \varepsilon_\alpha^{1/3}, \tag{B 30}$$

which corresponds to the following expression for μ_d in the asymptotic limit for large Pe

$$-\mu_d = K_1 \left(\frac{K_0}{K_1}\right)^{1/3} \varepsilon_\alpha^{1/3} \sim Pe^{-1/3}. \tag{B 31}$$

Equation (B 31) provides a theoretical explanation (by assuming the validity of the localization ansatz) of the exponent $\gamma = 1/3$ observed for $\Omega = (-1, 1)$ independently of κ.

The analysis developed in Appendix B can be generalized to the local behaviour of $w(\rho)$ and $V_{\text{ef}}(\rho)$ near the localization point ρ^* expressed by (5.4), By performing calculations identical to those developed in Appendix B one obtains in this case for γ the expression (5.5).

REFERENCES

Ananthakrishnan, V., Gill, W. N. & Barduhn, A. J. 1965 Laminar dispersion in capillaries. Part I. Mathematical analysis. *AIChE J.* **11**, 1063–1072.

Aref, H. 1984 Stirring by chaotic advection. *J. Fluid Mech.* **143**, 1–21.

Aris, R. 1956 On the dispersion of a solute in a fluid flowing through a tube. *Proc. R. Soc.* A **235**, 67–77.

Bajer, K., Bassom, A. P. & Gilbert, A. D. 2001 Accelerated diffusion in the centre of a vortex. *J. Fluid Mech.* **437**, 395–411.

Baldyga, J. & Bourne, J. R. 1999 *Turbulent Mixing and Chemical Reactions.* Wiley & Sons.

Beebe, D. J., Mensing, G. A. & Walker, G. M. 2002 Physics and applications of microfluidics in biology. *Annu. Rev. Biomed. Engng* **4**, 261–286.

Beigie, D., Leonard, A. & Wiggins, S. Invariant manifold templates for chaotic advection. *Chaos Solitons Fractals* **4**, 749–868.

Bensoussan, A., Lions, J.-L. & Papanicolau, G. 1978 *Asymptotic Analysis for Periodic Structures.* North-Holland.

Bohm, D. 1952 A suggested interpretation of the quantum theory in terms of "hidden" variables. I. *Phys. Rev.* **85**, 166–179.

Boyland, P. L., Aref, H. & Stremler, M. A. 2000 Topological fluid mechanics of stirring. *J. Fluid Mech.* **403**, 277–304.

Castelain, C., Mokrani, A., Legentilhomme, P. & Peerhossaini, H. 1997 Residence time distribution in twisted pipe flows: helical coiled system and chaotic system. *Exp. Fluids* **22**, 359–368.

Cerbelli, S., Vitacolonna, V., Adrover, A. & Giona, M. 2004 Eigenvalue-eigenfunction analysis of infinitely fast reactions and micromixing regimes in regular and chaotic bounded flows. *Chem. Engng Sci.* **59**, 2125–2144.

Childress, S. & Gilbert, A. D. 1995 *Stretch, Twist and Fold: The Fast Dynamo.* Springer.

Danckwerts, P. V. 1953 Continuous flow systems. *Chem. Engng Sci.* **2**, 1–13.

Danckwerts, P. V. 1958 The effect of incomplete mixing on homogeneous reactions. *Chem. Engng Sci.* **8**, 93–102.

Fannjiang, A. & Papanicolaou, G. 1994 Convection enhanced diffusion for periodic flows. *SIAM J. Appl. Math.* **54**, 333–408.

Giona, M., Adrover, A. & Cerbelli, S. 2005 On the use of the pulsed-convection approach for modelling advection–diffusion in chaotic flows – a prototypical example and direct numerical simulations. *Physica* A **348**, 37–73.

Giona, M., Adrover, A. & Cerbelli, S. 2009 Spectral analysis of the weighted Laplacian in slip and no-slip flows, *Phys. Rev.* E (submitted).

Giona, M. Cerbelli, S. & Creta, F. 2008 Spectral properties and universal behaviour of advecting–diffusing scalar fields in finite-length channels. *J. Fluid Mech.* **612**, 387–406.

Giona, M., Cerbelli, S. & Vitacolonna, V. 2004*a* Spectral properties and transport mechanisms of partially chaotic bounded flows in the presence of diffusion. *Phys. Rev. Lett.* **92**, 114101.

Giona, M., Cerbelli, S. & Vitacolonna, V. 2004*b* Universality and imaginary potentials in advection–diffusion equations in closed flows. *J. Fluid Mech.* **513**, 221–237.

Giona, M., Vitacolonna, V., Cerbelli, S. & Adrover, A. 2004*c* Advection–diffusion in non-chaotic closed flows: non-Hermitian operators, universality and localization. *Phys. Rev.* E **70**, 046224 I–XII.

Gleeson, J. P. 2005 Transient micromixing: examples of laminar and chaotic stirring. *Phys. Fluids* **17**, 100614.

Gleeson, J. P., Roche, O. M., West, J. & Gelb, A. 2004 Modelling annular micromixers. *SIAM J. Appl. Math.* **64**, 1294–1310.

Hardt, S., Drese, K. S., Hessel, V. & Schönfeld, F. 2005 Passive micromixers for applications in the microreactor and μTAS fields. *Microfluid Nanofluid* **1**, 108–118.

Ho, C.-M. & Tai, Y.-C. 1998 Micro-electro-mechanical systems (MEMS) and fluid flows. *Annu. Rev. Fluid Mech.* **30**, 579–612.

Hobbs, D. M. & Muzzio, F. J. 1998 Optimization of static mixer using dynamical system techniques. *Chem. Engng Sci.* **53**, 3199–3213.

Jen, C.-P., Wu, C.-Y., Lin, Y.-C. & Wu, C.-Y. 2003 Design and simulation of the micromixer with chaotic advection in twisted microchannels. *Lab on a Chip* **3**, 77–81.

Karniandakis, G., Beskok, A. & Aluru, N. 2005 *Microflows and Nanoflows*. Springer.

Kim, H. J. K. & Beskok, A. 2007 Quantification of chaotic strength and mixing in a micro fluidic system. *J. Micromech. Microengng* **17**, 2197–2210.

Kim, D. S., Lee, S. H., Kwon, T. H. & Ahn, C. H. 2005 A serpentine laminating micromixer combining splitting/recombination and advection. *Lab on a Chip* **5**, 739–747.

Liu, W. & Haller, G. 2004 Inertial manifolds and completeness of eigenmodes for unsteady magnetic dynamos. *Physica* D **194**, 297–319.

Liu, W. & Haller, G. 2004 Strange eigenmodes and decay of variance in the mixing of diffusive tracers. *Physica* D **188**, 1–39.

Majda, A. J. & Kramer, P. R. 1999 Simplified models for turbulent diffusion: theory, numerical modelling and physical phenomena. *Phys. Rep.* **314**, 237–574.

Metcalfe, G., Rudman, M., Brydon, A., Graham, L. J. W. & Hamilton, R. 2006 Composing chaos: an experimental and numerical study of an open duct mixing flow. *AIChE J.* **52**, 9–28.

Nguyen, N.-T. & Wereley, S. T. 2006 *Fundamentals and Applications of Microfluidics*. Artech House.

Nguyen, N.-T. & Wu, Z. 2005 Micromixers – a review. *J. Micromech. Microengng* **15**, R1–R16.

Pelesko, J. A. & Bernstein, D. H. 2003 *Modelling MEMS and NEMS*. CRC.

Perugini, D., Poli, G. & Mazzuoli, R. 2003 Chaotic advection, fractals and diffusion during mixing of magmas: evidence from lava flows. *J. Volcanol. Geotherm. Res.* **124**, 255–279.

Pikovsky, A., & Popovich, O. 2003, Persistent patterns in deterministic mixing flows. *Europhys. Lett.* **61**, 625–631.

Raynal, F., Beuf, A., Plaza, F., Scott, J., Carriere, P., Cabrera, M., Cloarec, J.-P. & Souteyrand, E. 2007 Towards better DNA chip hybridization using chaotic advection. *Phys. Fluids* **19**, 017112.

Rhines, P. B. & Young, W. R. 1983 How rapidly is a passive scalar mixed within closed streamlines? *J. Fluid Mech.* **133**, 133–145.

Salmon, J.-B. & Ajdari, A. 2007 Transverse transport of solutes between co-flowing pressure-driven streams for microfluidic studies of diffusion/reaction processes. *J. Appl. Phys.* **101**, 074902 1–7.

Scheuring, I., Karolyi, G., Pentek, A., Tel, T. & Toroczkai, Z. 2000 A model for resolving the plankton paradox: coexistence in open flows. *Freshwater Biol.* **45**, 123–132.

Scheuring, I., Karolyi, G., Toroczkai, Z., Tel, T. & Pentek, A. 2003 Competing populations in flows with chaotic mixing. *Theor. Popul. Biol.* **63**, 77–90.

Schmid, P. J. & Henningson, D. S. 2001 *Stability and Transition in Shear Flows*. Springer.

Shepherd, T. G., Koshyk, J. G. & Ngan, K. 2000 On the nature of large-scale mixing in the stratosphere and mesosphere. *J. Geophys. Res.* **105**, 12433–12446.

Squires, T. M. & Quake, S. R. 2005 Microfluidics: fluid physics at the nanonliter scale. *Rev. Mod. Phys.* **77**, 977–1026.

Straube, A. V. & Pikovsky, A. 2007 Mixing-induced global modes in open active flows. *Phys. Rev. Lett.* **99**, 184503.

Sukhatme, J. & Pierrehumbert, R. T. 2002 Decay of passive scalars under the action of single scale smooth velocity fields in bounded domains: from non self-similar probability distribution functions to self-similar eigenmodes. *Phys. Rev.* E **66**, 056302.

Szalai, E. & Muzzio, F. J. 2003 Fundamental approach to the design and optimization of static mixers. *AIChE J.* **49**, 2687–2699.

Taylor, G. 1953 Dispersion of soluble matter in a solvent flowing slowly through a tube. *Proc. R. Soc.* A **219**, 186–203.

Tel, T., de Moura, A., Grebogi, C., Karolyi, G. 2005 Chemical and biological activity in open flows: a dynamical system approach. *Phys. Rep.* **413**, 91–196.

Thyagaraja, A., Loureiro, N. & Knight, P. J. 2002 Spectral and evolutionary analysis of the advection–diffusion equations and the shear flow paradigm. *J. Plasma Phys.* **68**, 363–388.

Toussaint, V., Carriere, P. & Raynal, F. 1995 A numerical Eulerian approach to mixing by chaotic advection. *Phys. Fluids* **7**, 2587–2600.

Toussaint, V., Carriere, P., Scott, J. & Gence, J.-N. 2000 Spectral decay of a passive scalar in chaotic mixing. *Phys. Fluids* **12**, 2834–2844.

Trachsel, F., Günther, A., Khan, S. & Jensen, K. F. 2005 Measurement of residence time distribution in microfluidic systems. *Chem. Engng Sci.* **60**, 5729–5737.

Voth, G. A., Haller, G. & Gollub, J. P. 2002 Experimental measurements of stretching fields in fluid mixing. *Phys. Rev. Lett.* **88**, 254–501.

Wu, Z. & Nguyen, N.-T. 2005 Convective–diffusive transport in parallel lamination micromixers. *Microfluid Nanofluid* **1**, 208–217.

Zwietering, T. N. 1959 The degree of mixing in continuous flow systems. *Chem. Engng Sci.* **11**, 1–15.